Di Naccio Deborah (Orcid ID: 0000-0002-0344-1173)
Kastelic Vanja (Orcid ID: 0000-0002-7751-0055)
Carafa Michele, M. C. (Orcid ID: 0000-0001-5463-463X)
Milillo Pietro (Orcid ID: 0000-0002-1171-3976)

Gravity versus Tectonics: the case of 2016 Amatrice and Norcia (central Italy) earthquakes surface coseismic fractures

D. Di Naccio[1], V. Kastelic[1], M. M. C. Carafa[1], C. Esposito[2], P. Milillo[3], and C. Di Lorenzo[1]

[1]Istituto Nazionale di Geofisica e Vulcanologia, Sezione di Sismologia e Tettonofisica, L'Aquila, Italy.

[2]Department of Earth Science and Research Center for Geological Risks (CERI), Sapienza University, Rome, Italy.

[3]NASA Jet Propulsion Laboratory, California Institute of Technology, 4800 Oak Grove Drive, 91109 Pasadena (CA), USA

.

Corresponding author: Deborah Di Naccio (deborah.dinaccio@ingv.it)

Key Points:

- We assess the topographic and rheological influences on coseismic surface deformation along Mt. Vettore after the 2016 earthquake sequence
- The largest coseismic offsets occurred in the most unstable zones of Mt. Vettore, indicating potentially significant non-tectonic deformation.
- The coseismic fractures in the Piano Grande were not affected by topography or rheology contrasts, supporting a tectonic origin

This article has been accepted for publication and undergone full peer review but has not been through the copyediting, typesetting, pagination and proofreading process which may lead to differences between this version and the Version of Record. Please cite this article as doi: 10.1029/2018JF004762

Abstract

The 2016 central Apennines earthquake sequence was caused by slip on an extensional fault system and resulted in sizable coseismic surface deformation. The most evident effects occurred along the western slope of Mt. Vettore, a geologically and morphologically complex mountain ridge. Steep topography and rheological contrasts are known to have strongly controlled the coseismic deformation pattern during a number of different earthquakes that occurred in mountainous areas worldwide. Nevertheless, so far the role of seismically induced slope failures has not been taken into account in the interpretation of the surface fractures caused by the 2016 earthquake sequence.

We modeled the static and dynamic slope stability along the western flank of Mt. Vettore and in the underlying Piano Grande plain. Combining the slope stability analysis with geomorphic and geological analyses, we show that the coseismic fractures are distributed along the most unstable areas of the western flank of Mt. Vettore and can be partly explained by shaking-induced mechanisms such as gravity-driven displacement, compaction, and secondary ground failure. Conversely, in the Piano Grande plain the fracture pattern is not affected by topography or rheology contrasts, suggesting that it is positively caused by tectonic faulting.

Different processes, such as gravitational and erosional-depositional phenomena, may contribute to the exposure of fault scarps both during the coseismic and interseismic periods. Attributing the surface deformation entirely to tectonic faulting, especially in complex mountainous terrains such as the Apennines, may lead to an incorrect assessment of fault displacement and fault slip rate, and hence of sesimic hazard.

1. Introduction

Moderate to strong crustal earthquakes may generate surface fractures that are directly related to the ongoing tectonic processes, but also secondary effects due to ground shaking. Primary surface faulting indicates the propagation of the earthquake causative fault up to the ground surface, resulting in exposed surface fractures/fault planes, either reactivated or newly formed. Conversely, secondary coseismic effects consist of material remobilization, gravity-driven displacement and landslides (both re-activations and first-generation failures), and have been extensively reported as especially significant following earthquakes that occurred in high topography regions. The 1989 Loma Prieta (Cotton et al., 1990; Keefer, 2000), 1994 Northridge (Pradel et al., 2005), 1999 Chi-Chi (Chen et al., 2004) and 2008 Wenchuan (Chen et al. 2012) earthquakes are just some of the most notable examples.

Secondary coseismic effects are induced by earthquake acceleration that exceeds a threshold value (critical acceleration), such that the shear stress exceeds the shear strength on a pre-existing or newly formed shear plane. The main factors affecting slope stability are the local peak acceleration, earthquake magnitude, slope steepness, and degree of degradation of the lithologies involved (e.g. Keefer, 2000; Chen et al., 2004, Khazai and Sitar, 2004). In the 2008 Wenchuan earthquake, large landslides occurred above the region of maximum coseismic fault slip and were mainly driven by strong rheological contrasts (Chen et al., 2012). For the same earthquake, collapses and slide-forming tension cracks developed in the upper slopes, while the lower parts of the same slopes remained undeformed (Wang et al., 2010). In the 2013 Lushan and the 2015 Gorkha earthquakes the occurrence of landslides was strongly correlated with the geometry of the causative fault and of rupture propagation (Xu et al., 2015; Roback et al., 2018).

The Apennines have a long history of earthquake-induced landslides and other secondary coseismic phenomena. For this mountainous region, the CEDIT catalogue of coseismic secondary effects (Fortunato et al., 2012) reports numerous earthquake-induced landslides. For the same region, the CFTI5Med catalogue (Guidoboni et al., 2018) lists 527 testimonies for the specific category "landslide, earth-flow, mud-flow", referring to a number of earthquakes that caused significant modifications of the landscape.

The 2016 central Italy earthquake sequence is the most recent of these highly impacting events (Figure 1a). It was generated by a 60 km-long extensional fault system (e.g. Chiaraluce et al., 2017). The sequence started off on 24 August with a M_w 6.0 shock, commonly referred to as the Amatrice earthquake after the town that was totally destroyed by the event. On 26 October, two further damaging shocks (M_w 5.4 and M_w 5.9) occurred at the northern end of the aftershock sequence near the town of Visso. Four days later, on 30 October 2016, a M_w 6.5 shock, the strongest of the entire sequence, occurred in the central part of the area affected by sequence near the town of Norcia, with surface deformation extending over areas already affected by the previous main events.

Following the Amatrice earthquake, several newly formed fractures and rejuvenated bedrock fault scarps were reported at various heights along the western flank of Mt. Vettore and in the underlying Piano Grande basin (Figure 1b and Figures 2a-e; see also photographs of Emergeo WG, 2017a). According to the prevailing opinion (Emergeo WG, 2016; Lavecchia et al., 2016; Perouse et al., 2018, Pizzi et al., 2017, among others), all the observed surface deformation results from the propagation of the main earthquake rupture up to the surface, corresponding with the Cordone del Vettore fault, and should hence be interpreted as primary surface faulting. Other researchers (Bonini et al., 2016; Valensise et al., 2016) contended that the causative fault for the 2016 earthquake sequence is an inverted, shallow dipping thrust, and that the steep Cordone del Vettore fault is a secondary feature. Other researchers pointed out that the surface displacement seen after the Amatrice earthquake along the western flank of Mt. Vettore is disconnected from the primary coseismic subsidence (Gruppo di lavoro IREA-CNR & INGV, 2016; Polcari et al., 2017), interpreting it as partially (Albano et al., 2016) or entirely (Gispert Busquets, 2016; Huang et al. 2017) due to landslide displacement. Most of the surface fractures caused by the Amatrice shock were rather suspiciously observed along the western flank of Mt. Vettore, where selective erosion and gravity-driven movements have been reported in pre-earthquake literature (e.g. Giovagnotti, 1979; Coltorti & Farabollini, 1995).

Field observations show that the Norcia earthquake perturbed again the area previously deformed in the Amatrice event (especially the western flank of Mt. Vettore), but extended it further to the north (Figure 1, Figure 2a and Figures 2f-l; see also photographs of Emergeo WG, 2017b). Fractures and bedrock fault scarps associated with the Amatrice earthquake along the Mt. Vettore slope were rejuvenated and increased their offset almost tenfold. Besides that, newly formed fractures were observed in the Piano Grande basin (Figures 2j-k), along the western flank of Mt. Vettore and Mt. Porche – Mt. Bove (Figure 1a; Emergeo WG, 2017b; Villani et al. 2018).

Along the steep slopes and in loose deposits, the fractures were often seen organized in arcuate shapes, both following the Amatrice and - to a larger extent - the Norcia earthquakes (Figure 2). This configuration indicates shallow-seated downslope movements that cannot be straightforwardly related to surface faulting (Rogers & Chung, 2016). Franke et al. (2017) identified and interpreted some of the fissures, cracks and scarps caused by the Norcia earthquake in the slope deposits seen along the western flank of Mt. Vettore as due to slope instabilities, and separated them from tectonic fault ruptures.

To shed light on the role of steep topography and rheological heterogeneities during the 2016 central Italy earthquake sequence, we analyzed in detail the Piano Grande basin and the western flank of Mt. Vettore, where selective erosional processes and landslide movements have been extensively recognized and described before the earthquake sequence. To this end, we first analyzed three pre-earthquake aerial ortho-photographs, confirming the presence of gravity-induced deformation (see Section 3). We then analyzed the surface fracture database available for both the Amatrice and Norcia earthquakes to properly assess the spatial variability of the observed offsets along the western flank of Mt. Vettore and in the underlying Piano Grande (Section 4). Finally, we modeled the slope stability in static and pseudo-dynamic conditions to constrain the geomechanical model of the slope and assess any seismically-induced landslide displacement (Section 5). We show that a significant fraction of the surface offsets measured after the Amatrice and Norcia earthquakes can be explained simply as the effect of gravity- and rheology-driven processes (Section 6).

2. Structural setting in the Mt. Vettore

The 2016 earthquake sequence was caused by slip on a 60-km long extensional fault system running along the axis of the central Apennines from Visso to Amatrice (e.g. Chiaraluce et al., 2017; Figure 1a). On the basis of surface geology, different fault traces have been mapped in the area, altogether referred to as the Mt. Bove – Mt. Vettore – Mt. Gorzano fault system (Calamita et al., 1992; Galadini & Galli, 2003; Boncio et al., 2004).

The central Apennines are a thrust-and-fold belt, subjected to regional-scale uplift and NE-SW extension since Neogene-Quaternary time (Patacca et al., 1990; Lavecchia et al. 1994; Galadini & Galli, 2000; D'Agostino et al., 2001; Carafa & Bird, 2016). Individual mountain ridges are composed of Mesozoic-Cenozoic carbonate rocks and synorogenic flysch deposits, overlain by continental Quaternary deposits, including slope debris and colluvium-eluvium (hereinafter collectively referred to as SDCE), in their turn locally drapped by alluvial fan deposits (Figure 1). The area is characterized by a complex geomorphology featuring glacial and fluvial landforms, karst plateaus, and fluvio-lacustrine basins (Aringoli et al., 2014; Piacentini & Miccadei, 2014).

Different types of active landslide movements have been identified and described throughout the central Apennines (e.g. Di Luzio et al., 2004; Trigila et al., 2010; Esposito et al., 2013; Bianchi Fasani et al., 2014). In several instances the slope instabilities were seen to be closely related to steeply-dipping normal faults striking parallel to the local topography and placing the carbonate rocks in contact with loose slope deposits (Galadini, 2006).

Mt. Vettore is a Mesozoic carbonate ridge. Three main SW-dipping normal faults were recognized along its western flanks (e.g. Calamita et al., 1992; Brozzetti & Lavecchia, 1994; Pizzi & Galadini, 2009; Pierantoni et al., 2013), whereas the Piano Grande fault (hereafter referred to as PGF) has been detected in paleosesimological trenches located further to the west, in the alluvial fans of the Piano Grande (Galadini & Galli, 2003). The most evident of these three faults is the easternmost, named Cordone del Vettore fault (CVF) (e.g. Calamita er al. 1992; Pierantoni et al. 2013), along which the footwall block limestone is in contact with slope debris and colluvium-eluvium in the hanging wall. A second fault splay has been mapped along the middle slopes of Mt. Vettore (hereinafter MSF) at the contact between a limestone block and the colluvium-eluvium (Calamita at al., 1992; Pierantoni et al. 2013). The third and longest fault splay (Calamita at al., 1992; Pierantoni et al. 2013), that lies at the foot of the Mt. Vettore main slope, did not show any evident coseismic reactivation during both Amatrice and Norcia earthquakes (Figure 1b). In contrast, coseismic surface

deformation has been observed in the Piano Grande basin, close to the fault observed by Galadini and Galli (2003) in a paleoseismological trench.

3. Geomorphological characteristics and analysis of Mt. Vettore western slope

Several gravity-driven mass movements and rheological contrasts play a crucial role in the evolution of the western flanks of Mt. Vettore (see Aringoli et al., 2010). To confirm previous findings and determine the exact position of the main gravity-driven mass movements, we first performed a 2D photo-geological interpretation based on the analysis of shadow, tone/color, texture, and pattern of panchromatic, ortho-rectified aerial photos taken in 1988 and 1994 (Figures S1a-b) and of a color ortho-rectified picture taken in 2000 (Figure S1c), all provided by the Italian Ministry for the Environment (http://www.pcn.minambiente.it/mattm/servizio-wms/, last accessed in October 2018). Only gravity-related landforms recognizable in all three photographs have been mapped, avoiding all not persistent landforms, some of which potentially related to the Colfiorito earthquake (M_w 6.0) that shook this region on 26 September 1997. We detected landslide-related linear landforms such as crowns, scarps and secondary escarpments, (Figure 3) some of which were described by Coltorti and Farabollini (1995) as landslide scree, stratified slope waste deposits and erosional escarpments.

The length of the main landslide crowns and scarps ranges from ~300 m to ~500 m, suggesting significant slope movements at least in terms of surface extent (Figure 3). A main landslide scarp, also recognized by Coltorti and Farabollini (1995) as bounding the stratified slope waste deposits, occurs very close to the CVF to the north of Cima del Redentore (Figure 1b, Figure 2 and Figure 3). Just to the south, another complex landslide has its crown at the contact with the MSF: it exhibits undulations and secondary scarps with small trenches downslope at about 1,600 m a.s.l. (Figure 2a and Figure 3). Notably, the lower section of this landslide is planar and cut by a slope-parallel trench (Figure 2a), described by Demangeot (1973) as a characteristic feature associated with earthquake-triggered landslides. Another landslide whose crown developed in the SDCE was recognized in the southern part of the Mt. Vettore (Figure 3).

Overall the geometrical pattern of landforms indicates translational sliding mechanisms; in their turn, the multiple scarps recognized along the slope indicate activity with multiple styles. This combined evidence suggests that Mt. Vettore has been exposed to an intense gravitational morphogenesis repeatedly and well before the 2016 earthquakes. We also identified other minor landforms, such as generic geomorphological lineaments and trench-like linear depressions, and interpreted them as due to shear and tensile stresses, respectively, acting on inherited structural, high angle anisotropies (i.e., faults and fractures). The internal layering of scree slopes which mantles a wide portion of the slope and the boundary at the contact with the bedrock has a rough planar shape nearly parallel to the slope topography. These planes represent relevant anisotropies that can act as preferential sliding planes favoring translational mechanisms within the unconsolidated debris cover or at the contact with the underlying bedrock.

Over time, different research teams recognized non-tectonic processes along the western slope of Mt. Vettore, including mass wasting slope features referred as “grassy steps” (a direct translation from the Italian "gradini erbosi"), identified by Giovagnotti (1979) as a characteristic local feature. Other processes such as rapid debris flows, deep gravitational slope movements and rockfalls were also described (e.g. Trigila et al.; 2010). Moreover, the massive limestone outcrop seen along the Mt. Vettore mid slope corresponds to a huge olistolith (Coltorti & Farabollini, 1995), and the MSF escarpment formed along its contact

with SDCE is likely due to both textural and lithological heterogeneity. Thus this contact zone is prone to exhibit secondary coseismic effects when submitted to ground shaking.

Besides the tectonic and gravity-driven activity, diffuse karst processes in the Piano Grande (e.g. Giovagnotti, 1979) and the effects of deforestation (e.g. Gentili & Pambianchi, 1989) have been described as concurring in accelerating and propagating slope erosion and rejuvenation, thus potentially increasing the instability of Mt. Vettore under seismic loading.

4. Coseismic fractures in the Mt. Vettore area after the Amatrice and Norcia earthquakes

Different teams surveyed the coseismic ground surface deformation along Mt. Vettore after both the Amatrice and Norcia earthquakes. For details on technical aspects of the surveys, we refer the reader to the papers by Emergeo WG (2016) and Villani et al. (2018). For the scope of our work, it is fundamental to point out that the fractures and offsets reported in these publications after the Norcia earthquake represent the cumulative effect of both earthquakes.

We elaborated the two available surface fracture databases (Emergeo WG, 2016; Villani et al., 2018) to extract the data surveyed along the western flank of Mt. Vettore and the underlying Piano Grande basin (Figure 1b). We retained the data identified as "ground fractures "and "bedrock free-faces" (the latter defined as the rejuvenated part of a preexisting fault scarp). Conversely, we discarded all entries displaying neither horizontal (HR) nor vertical offset (VR) and all multiple entries for the same geographic position (decimetric precision) having the same HR and VR values. We did not consider the HR values reported as zero for the Norcia earthquake if they were greater than zero for the Amatrice earthquake. In such cases, the estimation of the HR component following the Norcia earthquake is necessarily wrong and indicates a bias towards measuring only the VR component. Our final database resulted in 2,365 and 4,703 data records for the Amatrice and Norcia earthquakes, respectively.

Unfortunately, the offset measurements of both databases exhibit a selective feature-specific attention by their survey teams: the larger displacements were generally oversampled with respect to the smaller ones. When dealing with databases affected by such strong biases, a robust estimation of the spatial variability of the observed offsets cannot be based on simple arithmetic average, as clusters of large displacements would unrealistically dominate the results. Under these circumstances a more appropriate assessment of the spatial distribution of the observed displacement is the frequency analysis, which reduces any sampling bias of classical along-strike displacement profiles (McCalpin, 2009; Salisbury et al., 2015). In detail, we fitted HR, VR and the total component with a least square fitting function along five profiles roughly running N-S to NNW-SSE, i.e. parallel to the slope along the coseismic fracture pattern and covering the entire western flank of Mt. Vettore and the underlying Piano Grande (Figure 4 and Figure S2). In detail, we used the Chebyshev polynomials as the fitting function because this type of fit uses spectral information retrieved from the known points to determine the behavior along the whole profile (Arfken & Weber, 1995).

In the following, each of the five profiles along which we analyzed field data is identified as a string sx-profile (Figure 4 and Figure S2), with x ranging between 1 and 5 moving eastwards. The length of the sx-profiles depicts the maximum observed deformation zone resulting from the cumulative effects of the Amatrice and Norcia earthquakes. In the fracture analysis (e.g. Figures 5-6) we refer to all distances as measured from the northern tip of each trace (crossed points in Figure 4). It is important to point out that the deformation

zones, i.e. the sx-profiles, do not necessarily bound the fault traces that were mapped by earlier studies (e.g. Pierantoni et al., 2013). The fractures generally developed in the proximity of fault traces mapped before the earthquake sequence (Figure 1b) and they are often scattered in their footwalls and hanging walls.

To model the slope instability (see Section 5) we selected six profiles parallel to the maximum slope (Figure 4 and Figure S2). We labeled such modeled profiles as ry-profile, with y increasing southwards from 1 to 5.

We finally calculated the mean offset and the 90% confidence interval around 13 points located at the intersection of the sx- and ry-profiles; these offsets were then used to score our modeling results against field measurements. Each of these points is referred to as Pz-point, with z ranging between 1 and 13 (Figure 4).

The most continuous coseismic surface deformation was observed along the s4-profile roughly parallel to CVF (Figure 1b and Figure S2). Following the Amatrice earthquake, it was seen to extend for ~ 2.2 km from Mt. Vettoretto northwards (Figure 1b), and following the Norcia earthquake it further extended northwards for ~ 0.8 km with a more complex spatial distribution.

Although the mapped fractures are suggestive of a continuous exposure along the CVF, in several cases - and generally when they occur in loose continental deposits - they are arranged in individual arcuate, downward-concave semi-circular fractures (Figures 2d-e, Figure 2h and Figure 2l). Whitish bands of freshly-exposed, unaltered limestone were observed at the contact between SDCE and the bedrock fault plane (Figures 2b-c and Figures 2f-g), where the SDCE was generally toppled away and lowered up to 25 cm following the Amatrice earthquake and up to 200 cm following the Norcia earthquake. These bands are commonly referred to as "nastrini di faglia" ("fault ribbons") in the Italian geological literature.

The VR and HR offsets observed following the Amatrice earthquake had mean values in the range 6-17 cm (Figure 5a; analyzed data available in Table S1) and 1-19 cm (Figure 5b and Table S1), respectively. The resulting VR/HR ratio falls in the range 1-2, but is locally < 1 (e.g. ~2.6 km from the northern tip of the s4-profile in Figures 5a-b). The strike of the fractures varies from 70° to 225°, 95% of values falling in the 95°-180° range, and 75% in the range 120°-165°.

For the Norcia earthquake, the mean VR and HR offsets ranged from 8 to 153 cm (Figure 5d; analyzed data available in Table S2) and from 9 to 57 cm (Figure 5e and Table S2), respectively, with a VR/HR ratio in the range 1 to 5 (Figures 5d-e). Most of the fractures strike 110°-160°, thus perpendicular to the average slope direction, with clusters striking 160°- 210° (~20%), 50°- 110° (10%), and 260°- 350° (10%). The fracture zone (identified by the trace of the s4-profile) developed further northwards for ~ 0.8 km in the SDCE material (location indicated by an orange arrow in Figure 1b and Figure 2a, and by a red bar in Figures 5d-f). In this area the fractures mostly strike between 140° and 180°, with mean VR offset ranging between 8 and 83 cm (Figure 5d; analyzed data available in Table S2), HR between 8 and 37 cm (Figure 5e and Table S2), and VR/HR ratio < 1 close to the northern tip of the deformation zone (e.g. at ~0.2-0.3 km along the s4-profile in Figures 5d-e). At the point indicated by an orange arrow in Figures 1b and Figure 2a, a fracture zone with a roughly N-S orientation branched off from the general NW-SE oriented CVF fracture zone extending for ~ 2 km (s5-profile in Figure 4 and Figure S2). The fractures strike 180°-200° and exhibit mean VR values between 12 and 28 cm and mean HR values between 6 and 16 cm (Figure S3a-c and Table S3).

Around the Mt. Vettore mid-slope, the fracture zone (s2-profile in Figure 4 and Figure S2) developed along or in the hanging wall of the MSF fault splay, mainly in the SDCE (Figure 1b and Figure 2a). After the Amatrice earthquake, the total fracture zone extended within the SDCE for a total length of ~0.9 km (Figure 1b). The fractures were sporadic and only a few cm-long. VR and HR generally did not exceed 12 cm. A semi-circular shaped, 110 m-long fracture zone displaying a better spatial continuity was observed in the area around P11-point (Figure S2, Figure 2a and Figure 2e). In this area, the Norcia earthquake overprinted the surface deformation of the Amatrice earthquake (Figure 1b and Figure 2a). The fractures generally followed the MSF bedrock fault scarp along a 140° – 190° strike. The mean VR and HR offsets reached their maximum value of 87 cm (Figure 6a; analyzed data available in Table S4) and 50 cm (Figure 6b and Table S4), respectively, at ~ 1.6-1.7 km from the northern tip of the s2-profile (around P10-point). From 0 to ~ 1.3 km, the fracture zone developed in the SDCE (Figure 1b and red bar in Figures 6a-c) showing an even more complex geometry associated with the development of secondary fracture lineaments (Figure 2a, Figure 2h, and Figure 2l). The fractures were distributed in a downslope concave fashion as clearly seen in the spatial fracture pattern of this area (Figure 1b; Figure 2). The downslope concave arrangement of fractures is corroborated by the fracture orientation. The fractures strike southeast in the northern part of the deformation zone (average: 150°; median: 145°), south in the central part (average: 183°; median: 172°), and south-southwest in the southern part (average: 194°; median: 193°). The rest of the fractures along the s2 profile (the curvilinear part) formed along the southwestern contact between the carbonate block and the SDCE, and exhibit a southern strike (average 170°; median 169°); it must be pointed out, however, that the strike of the majority of fractures falls in the range 150°-200°, and that there exist scattered fractures covering the entire range of possible orientations. In this area, the mean VR and HR offsets exhibit maximum values of 97 cm (Figure 6a; analyzed data available in Table S4) and 47 cm (Figure 6b and Table S4), respectively, at ~1 km from the northern tip. All along the s2-profile, the VR/HR ratio ranges between 1 and 3 (Figures 6a-b). A secondary fracture zone developed at the northeastern contact between the olistolith and the SDCE (Figure 1b) over a length of ~ 0.9 km (s3-profile in Figure 4 and Figure S2). These fractures generally strike northwest, but sporadically also southeast and southwest. Fracture VR and HR mean values fall in the range 3 to 30 cm and 3 to 17 cm (Figures S3d-f and Table S5), respectively.

The Piano Grande fracture zone (s1-profile in Figure 4 and Figure S2) is located at the foothills of the western flank of Mt. Vettore. It developed within the alluvial fan, fluvio-lacustrine deposits and eluvium in the hanging wall of the fault identified through paleoseismic investigations (Galadini & Galli, 2003; Figure 1b). The ~1 km-long fracture zone caused by the Amatrice earthquake (Figure 2a) was characterized by sporadic, centimetric-size open fractures, generally showing no vertical offset (VR=0; $1 \leq HR \leq 3$ cm). The Norcia earthquake reactivated the fracture zone, overprinting the surface caused by the Amatrice earthquake. It extends in the N-S direction over a length of ~1.7 km (Figure 1b and Figure 2a). Specifically, near the southern end of the s1-profile and for ~1.3 km northward (Figures 6d-f), the fractures exhibit spatial continuity (see Figures 2j-k as an example), whereas further north they appear only sporadically. The fractures strike between 150°–200°, with mean VR and HR values ranging between 2 and 10 cm (Figure 6d; analyzed data available in Table S6) and between 2 and 4 cm (Figure 6e and Table S6), respectively, the VR/HR ratio being always close to 2 for the entire Piano Grande fracture zone.

We compared the maximum slope orientation (aspect map in Figure 7, Figure S4, and Table 2) along the Mt. Vettore and the dip direction of fractures measured after both Amatrice and Norcia earthquakes. We assumed that gravity-induced slip would occur in the

direction of maximum slope, and that the direction of observed slip is perpendicular to the measured strike of the fractures. This latter quantity is used as an approximation for the direction of displacement, given that no observations on slip vectors were systematically reported in the fracture databases.

We noticed a spatial correlation between the fracture dip direction and the maximum slope direction along the western flank of Mt. Vettore, suggesting that part of the coseismic deformation responds to a strictly topographic control.

5. Modeling the permanent earthquake-induced displacement

Based on the interpretation of aerial photos and on the analysis of coseismic fractures, we hypothesized the existence of significant non-tectonic coseismic displacements and modeled their occurrence. To test this hypothesis, we could count on a range of possible methodologies. The most powerful and sophisticated of these methodologies (e.g., stress-strain numerical models), however, require very detailed input data to fully exploit their potential. Unfortunately, site sampling and field-laboratory analyses of the Mt. Vettore outcrops are made difficult both by limitations in the accessibility of the sampling sites and by the sedimentological features of the sediments. For example, carrying out a geognostic campaign for both stratigraphic and geotechnical purposes is very hard in the high-mountain environment, due to the steep slopes and to the absence of suitable paths for transporting the instrumentation needed. In addition to that, the SDCE deposits, that are responsible for most of the observed landslides, are composed of blocks and boulders whose overall strength parameters cannot be measured by conventional laboratory apparatuses.

In consideration of these circumstances, we decided to perform a slope stability analysis under static and pseudo-static conditions based on simplified standard approaches (i.e. Limit Equilibrium Method - LEM and Newmark analysis) and on assumptions about the geomechanical model of the slope. We assumed that field observations coupled with expert judgement can provide a reliable, albeit simplified model of the slope. We used a two-layered geological model (see Table 1 and Text S1 for further details) formed by the carbonate bedrock (mainly fractured and stratified limestones of the Corniola Formation) and the overlying continental deposits (mainly grain-supported sediments of slope and colluvial environments; SDCE).

As for the basic geological input we relied on:

- the 1:40,000 geologic map published by Pierantoni et al. (2013);
- the 1:100,000 Geological Map of Italy (sheet 132-Norcia; Servizio Geologico di Stato, 1941);
- the 1:10,000 Geological map of the Umbria Region (Carta Geologica Regionale 1:10000; 2016);
- the geomorphological map of the Castelluccio di Norcia basin (Coltorti & Farabolini, 1995): and
- the structural map of Calamita et al. (1992).

The available data were integrated by field surveys and by our own interpretation of aerial photos (Figure 3). The 3D reconstruction of the geo-lithological layers was obtained from several cross sections perpendicular to the elongation of the relief through a kriging interpolation. The thickness of the SDCE (layer 1 in Table 1) gradually increases downslope towards the Piano Grande and does not exceed 25 m at around 0.2-0.3 km downslope from both the CVF and MSF, i.e. at the contact with the limestone (Table S7). Its maximum thickness, probably no more than ~ 50 m, can be inferred for the deposits cropping out in the northern part of slope (i.e. between the r1- and r3-profiles in Figure 4).

The rheological parameters were constrained adopting a multi-stage approach and assuming they are uniform in each layer (Table 1 and Text S1).

The shear strength of each layer is expressed by the cohesion (c) and by the angle of internal friction ϕ related to the shear τ and normal stress σ by the linear relation of the Mohr-Coulomb failure law:

$$\tau = c + \sigma \tan \phi \quad (1)$$

For the SDCE deposits (layer 1 in Table 1) we chose a range of realistic (i.e. available on technical literature) parameters for coarse grained deposits of angular gravels, blocks and boulders with poor or absent matrix, the latter being relevant for assessing the presence of cohesion (null or close to 0 in our case, see Table 1). The range of realistic ϕ has been constrained at the lower boundary, assuming to be roughly coincident with the angle of repose of debris deposits, which cannot be lower than the average slope angle (Figure 4 and Table 1). We used the unit weight volume (γ) parameter to assess the normal stress which is defined as $\sigma = \gamma H$, with H being the depth from the ground surface. The value of γ was inferred from the unit weight volume of carbonate rocks (24 and 28 kN/m^3; e.g. Esposito et al., 2007; Aringoli et al., 2010) and from the void ratio (ratio between volume of void and volume of solid) assuming little or absent matrix. For the carbonates (layer 2 in Table 1) we adopted the generalized Hoek-Brown criterion (Hoek & Brown, 1997; Hoek et al., 2002) which was derived by linear regression of Eq. 1. For further details on the geological model, the reader is referred to Text S1 and Table S7.

We calibrated the parameters by back-analyzing the slope stability in static and dry conditions, thus tuning them so as to fall in a realistic range, i.e. never resulting in Factor of Safety (FS) < 1 in this conditions. This is a strong constrain because the geometry of Mt. Vettore is stable under current ground-water conditions, and stable slopes should have FS values in excess of 1. At the same time, the parameter values at the upper boundary of the range should allow the slope to fail at least in wet conditions (i.e., with a pore pressure ratio greater than 0), in order to fit the geomorphological frame described by previous investigators (e.g. Coltorti & Farabollini, 1995) and by our interpretation of aerial-photographs. Finally, an additional criterion for filtering the parameter *via* back-analysis is the obvious consideration that the modeled displacements in dynamic condition should not exceed the observed displacement.

To investigate possible gravity-driven components in the observed offsets, we consider as the heads of potential unstable mass the northwest-striking CVF and MSF fault scarps, where limestones are placed in contact with the loose sediments. The nature and the thickness of the materials involved in the process (SDCE in Figure 1) and our aerial photo-interpretation suggest translational sliding movement with a potential critical failure surface confined into the continental deposits and a very low depth/length ratio (Varnes, 1978). We based the slope stability analysis on the rigorous method by Janbu (1973) using SSAP2010, Version 4.8.2 (Borselli, 2018), thus assuming landslide mass movement along a roughly planar surface with little rotation or backward tilting.

The 2D analysis was performed along six rx-profiles (Figure 4, Figure S2 and Section 3) best representing the different topographical and rheological conditions along the western flank of Mt. Vettore. We also tested the reliability of our gravity-driven modeling comparing the direction of the movement implied by Newmark's analysis (i.e. down slope along the strike of the ry-profiles) with the displacement observed in the field (see also Section 4). For both the Amatrice (Figure S4) and Norcia events (Figure 7), we find a very good correspondence between the maximum slope direction and the fracture dip direction: the

average mismatch in a 200 meter buffer zone around the Pz-points is 11.8° and 15.2° (Table 2), respectively for Amatrice and Norcia earthquake. We further note that the fracture dip direction does not show a systematic shift with respect to the aspect value. Rather, the fracture dip directions are scattered in the range N180° to N320° (see Figure S5).

We firstly performed the slope stability analysis under static and dry conditions, according to the Janbu's slice method. The slice method is a category of LEM ((Duncan, 1996; Krahn, 2003; Chowdhury et al., 2009) based on a portioning of the potentially unstable mass into different slices, bounded by vertical limits between the topographic surface and the assumed slip surface, and on the computation of the overall equilibrium (i.e. of the horizontal, vertical forces and/or moments) by applying appropriate equilibrium equations to each slice. The overall stability is assessed by equaling the resisting (mainly related to mechanical properties of the slope material and slope geometry) and driving forces (mainly related to the weight of slope materials, slope geometry and pore water pressures, if present). LEM does not consider the deformation of the potentially unstable rock/soil mass but only analyze the ratio between the forces, referred to as Factor of Safety (FS). If FS is ≥ 1, the considered slope section is in equilibrium, i.e. stable, as the overall strength of the slope exceeds the destabilizing forces. Conversely, FS < 1 means that the slope section is beyond its limit of equilibrium, i.e. unstable. If the location of the sliding surface is not known, as in our case, it can be found using numerical optimization methods (in this case, the software SSAP2010, Version 4.8.2), i.e. by analyzing several (up to thousands) potential sliding surfaces and identifying the one (or those) with lower values of FS. For our final solution, we retain 10 sliding surfaces with the minimum FS value. The geometries of the potential sliding surface (dip angle (α), length and depth) are extracted through images similar to that shown in Figure 8a and Figure 9a.

The 2D modeling highlights two low-FS zones (Figure 4). In the first zone, located in the northern area between the r1- and r3-profiles, FS falls in the range 1.13-1.14. Our aerial photo-interpretation (Section 3) shows that this portion of Mt. Vettore was an unstable area well before 2016 (Figure 3). It should also be noted that the spatial pattern of fractures observed following the Norcia earthquake fits perfectly the landslide crown derived from our aerial photo-interpretation (Figure 4). The second unstable area is located in the southern part of Mt. Vettore (between the r4- and r6-profiles in Figure 4), where FS is in the range 1.1-1.2 range. Also in this area our aerial photo-interpretation revealed the existence of a major pre-2016 main landslide (Figure 4). Notably, the landslide crown developed in the SDCE (Figures 1b) next to the area along the s4-profile where the maximum offset was observed following both the Amatrice (around P5-point in Figure 5c; see also Table S1 for the analyzed offset data) and the Norcia earthquakes (Figure 5f; see also Table S2).

The critical failure surfaces derived from the slope stability analysis (see as example the pink lines in Figure 8a and Figure 9a) along all rx-profiles have a dip of $27° \leq \alpha \leq 35°$; they are confined within the slope deposits (not exceeding 25 m thickness in the zone highlighted by the critical failure surfaces) and reach a maximum depth of ~15 m for the unstable masses running roughly parallel to CVF and ~8 m for that partially running parallel to MSF (see as example Figure 8a and Figure 9a). On the one hand, the depth/length ratio of the potential critical failure surfaces is very low (less than 0.1), indicating translational movements (Varnes, 1978). On the other hand, the area around the s1-profile, partially corresponding with PGF (around the P12- and P13-points; Figure 4 and Figure 8a) is not affected by slope instabilities (slope less than 3°).

Using the FS and the dip angle (α) of the critical failure surfaces (as an example, see the pink lines in Figure 8a and Figure 9a) determined in the LEM analysis, we used the

Newmark method (1965) to assess the seismic loading caused by both the Amatrice and Norcia earthquakes (for example, see Figures 8b-d and Figures 9b-d). Our goal was to assess the displacement potentially associated with shaking and gravity-induced movement. We chose the Newmark method for its simplicity, being aware that more complex techniques (such as the stress-deformation analysis) could reproduce more precisely the expected slope behavior. More specifically, the Newmark method calculates the displacement of a sliding rigid block based on two inputs: the record of seismic ground acceleration as a function of time ($a(t)$), and the landslide critical acceleration (a_c). The theory behind the Newmark method assumes that a potentially unstable block will slide along a yield surface every time the earthquake acceleration exceeds a_c. Integration of the critical portions of the acceleration pulses gives the velocity-time history of the block, and the integration of the velocity pulses results in a cumulative displacement (Figure 10).

From a mechanical point of view, for ground acceleration greater than a_c the shear stress on the yield surface exceeds the shear strength of the material and the potential unstable block begins to move. Thus, a_c may be related to the material rheology and sliding surface geometry (Jibson, 1993; 2011); for the case of a translational failure, it is defined as:

$$a_c = (FS - 1) \cdot g \cdot \sin(\alpha); \quad (2)$$

where g is the gravitational acceleration.

Based on the results of our LEM analysis, we subsequently solved equation (2) with critical failure surfaces α varying between 27° and 35° at 0.5° incremental steps, and with FS at 0.01 incremental steps. The obtained critical acceleration a_c values vary between 0.014 and 0.340 g (Figure 10a).

We determined the shaking and gravity-induced displacement (D_{MOD}) in the whole range of a_c modeled along all the ry-profiles (see Figure 4) and for the seismic loading caused by both the Amatrice and Norcia earthquakes using the Slammer software ("Seismic LAndslide Movement Modeled using Earthquake Records"; Jibson et al., 2013), thus not considering any potential wave amplification due to topographic site effects. To select the most appropriate accelerograms for the Amatrice and Norcia earthquakes, we first chose stations within a 15 km radius from the target area, which resulted in seven three-component accelerograms of the Italian Strong Motion Network and of the Italian National Seismic Network (Figure 1 and Table 3; Luzi et al., 2016). We then considered the location of the accelerometers with respect to the causative faults of the Amatrice and Norcia earthquakes. As the western flank of Mt. Vettore lies in the hanging wall of the seismogenic fault system of both 2016-earthquakes (e.g. Chiaraluce et al., 2017), we discarded all stations falling on turbiditic siliciclastic sediments of the footwall (see column "Fault position" in Table 3). To avoid possible local effects, we considered the lithotechnical properties and topographic setting at each site of the four remaining stations (see columns "Geological unit", "Soil class" and "Topographic class" in Table 3), finally choosing the records of NRC for the Amatrice earthquake and of CLO for the Norcia earthquake. Station CLO lies on the carbonates cropping out in the western portion of the Piano Grande plain, while NRC lies on the continental deposits of the Norcia basin further to the west (Figure 1). We used both the E-W and N-S components of the NRC and CLO strong-motion records to determine the two relative maximum gravity-induced displacement (D_{MOD}), applying a dynamic force nearly parallel to the direction of maximum slope (Jibson, 2011). In this way, for each ry-profile, the minimum angular mismatch between strike and E-W or N-S component is less than 30°,

which allows a first, though rough, estimation of gravity-induced displacement with the Newmark analysis. The resulting D_{MOD} are comparable for both components and for both earthquakes (Figure 10a) thus not influencing substantially any further analysis. In both cases the resulting displacements exceeded the collapse thresholds values (~10 cm) suggested for soil deposits (Romeo, 2000).

For the Norcia earthquake, the modeled gravity-induced displacements D_{MOD} were obtained summing up the modeled dislocations resulting from seismic loading of both earthquakes (that is to say, using the NRC and CLO strong motion data in the Newmark analysis, see Figure 10a). This procedure allows the D_{MOD} to be compared with the cumulative displacement (D_{OBS}) measured in the field after the Norcia earthquake (Figures 8c-d, Figures 9c-d and Section 3).

As expected, the D_{MOD} shows the largest values (Figures 8b-d and Figure 9b-d) in the two most unstable areas of Mt. Vettore (highlighted by the r2- and r5-profiles, Figure 4). In detail, for the northernmost unstable area along the s4 fracture zone, D_{MOD} reaches the maximum value of 13 cm and 70 cm, respectively for the Amatrice and Norcia earthquakes (yellow points in Figures 8b-c and around P2-point in Figures 11c-d). At the P8-point, close to the complex arcuate-fracture zone in the SDCE (Figure 4), the maximum D_{MOD} is 70 cm (yellow point in Figure 8d and Figure 11b) for the Norcia earthquake. Along the s4-fracture zone (P5-point), the D_{MOD} can attain 35 cm and 200 cm, respectively for the Amatrice and Norcia earthquakes (Figures 9b-c and Figures 11c-d). Along the s2 fracture zone (P11-point) D_{MOD} can be up to 110 cm (Figure 9d and Figure 11b) for the Norcia earthquake.

Remarkably, along the western slope of Mt. Vettore, we notice a rough coincidence between the maximum values attained by D_{MOD} and D_{OBS} (i.e. around the P2-, P5-, P8- and P11-points in Figures 11b-d and Figures S6-7); in particular, D_{MOD} is seen to increase around the two most unstable zones detected by aerial photo interpretation (respectively between the r1- and r3-profiles and between the r4- and r6-profiles in Figure 4). In the southern zone (i.e. around P5- P6- and P11 points in Figures 11b-d and Figures S6-7), assuming that the modeled gravity-driven displacement can not be larger than the observed field displacement ($D_{MOD}<D_{OBS}$), the data comparison highlights a continental deposit with frictional angle probably higher than 33° or more cohesive. Conversely, along the s1-profile, the flat topography and the absence of a significant rheological contrast at the surface (Figure 8a) allowed us to rule out gravity-driven mechanisms as the main cause of the observed dislocation (Figure 11a).

A further interesting result of the Newmark analysis is the determination of gravity-induced displacements during the earthquake loading. This evolution of shaking-induced displacement can be directly compared with available geodetic data. Figure 10 shows the time necessary to yield the largest part of the cumulated permanent gravity-driven displacement (D_{MOD} in Figures 10b-c) for both earthquakes. In detail, for the Amatrice earthquake, the complete gravity-driven displacement (i.e. the flat zone in the displacement-time history graphs of Figure 10b) is predicted to initiate ~2.0 seconds (Figure 10b and Figure 10d) after the first seismic wave arrival (NRC accelerogram) and to last over ~3 seconds. For the Norcia earthquake, the gravity-induced displacement started ~1.5 seconds after the first arrival (CLO accelerogram) and lasted ~6 seconds (Figures 10c-d).

6. Discussion

The Amatrice and Norcia earthquakes caused extensive ground modifications over a wide range of deformation styles, with the western slopes of Mt. Vettore best representing

this complexity. Surface faulting is only one aspect of the coseismic process, as the effects of steep topography and rheological contrasts, especially in steep mountainous areas, play an important role in the overall deformation pattern. The role of non-tectonic coseismic deformation may even become dominant, as extensively documented over the past two decades (e.g. Keefer, 2000; Khazai and Sitar, 2004; Chen et al., 2012; Roback et al., 2018). Thus, a negligible or absent role of topography or rheology in the surface deformation pattern of 2016 Central Apennines earthquake sequence would sound rather unrealistic. Surprisingly, so far this aspect has not been addressed properly for this important earthquake sequence, and our results challenge the prevailing (and often dogmatic) allegation that the observed surface fractures were exclusively and unambiguously due to primary tectonic faulting.

The slope stability and Newmark analyses performed in this study suggest that topography and rheology influenced the coseismic displacement along the western flank of Mt. Vettore (Figure 11). Our findings confirm several available observations, that have been often neglected or marginalized to magnify the role of primary faulting. For example, Franke et al. (2017) documented slope failures, rock falls and soil compaction along the western flank of Mt. Vettore after the Norcia earthquake, clearly separating non-tectonic fractures from tectonic fault ruptures. They also recognized tectonic and shaking-induced phenomena acting together, especially in very steep areas. Non-tectonic movements were described and modeled also by Gispert Busquets (2016), Huang et al. (2017) and Polcari et al. (2017) for the Amatrice earthquake.

Our results show that the range of possible gravity-related displacements along the western flank of Mt. Vettore is rather ample due to some important sources of uncertainty. Given the absence of on-site sampling along Mt. Vettore and of field-laboratory analyses, rheological parameters and elastic properties are the main source of uncertainty for our model. We decided to reduce these potentially large uncertainties by testing rheological values of cohesionless gravel deposits or with little content of clay matrix (cohesion of 5 kPa) with static stable slope (FS > 1) as boundary conditions. It must be stressed that the amount of coseismic offset due to shaking-induced processes may further increase considering the soil densification of the granular talus deposits: a further highly elusive rheological characteristic in loose deposits and steep slope topography.

Another source of uncertainty is the angular mismatch between the strike direction of our ry-profiles and the main components of strong motion used in the Newmark analysis. The optimal estimation of gravity-induced displacement would require using *ad hoc*-generated synthetic seismograms along the strike of the ry-profiles, whereas we approximated them with the E-W and N-S components of strong motions. For each ry-profile, however, the maximum angular mismatch between strike and E-W/N-S component is less than 30° on average, which certainly allows a first - albeit rough - estimation of gravity-induced displacement.

Having accounted for all of the above sources of uncertainties, we maintain that a gravity-induced signal is still recognizable in the observed coseismic deformation field; this signal is further enhanced for cohesionless and/or low frictional angle gravel deposits. For the southern portion of the western flank of Mt. Vettore, the data comparison highlights that a continental deposit with frictional angle larger than 34° or more cohesive (i.e. with the boundary condition of $D_{MOD}<D_{OBS}$) can account for the total measured displacement.

Wilkinson et al. (2017) reported that the surface motion of the western flank of Mt. Vettore occurred within 2-4 seconds after the first arrival of the seismic wave radiated by the 30 October 2016 Norcia earthquake. The authors concluded that such short-time interval unambiguously dismisses any shaking-induced contribution to the observed deformation

pattern. Such reasoning can be put on test by the Newmark analysis performed in Section 5. Our results (see Figure 11c) show that pure gravity-driven displacements along the western slopes of Mt. Vettore could have started in the same short time interval after the earthquake onset (~1-2 seconds) and occurred within the same time lapse (5-6 s) reported in Wilkinson et al. (2017). Thus, primary faulting is not the only process that can cause surface deformation in such short time frame.

The spatial pattern of fractures, including their orientation, continuity and coherence, was seen by many as the main evidence for interpreting them exclusively as resulting from surface faulting along Mt. Vettore (Emergeo WG, 2016; Lavecchia et al., 2016; Perouse et al., 2018, among others). Following our field work and our close inspection of all available photographic material (Figure 2 and Emergeo WG, 2017a and 2017b), however, we remark that the coseismic ground deformation responds to a strong structural and rheological control, with a loss of slope continuation in SDCE or a collapse of the same deposits where in contact with limestone.

With their greatest slope angles and sharper lithological boundaries, the s4- and s2-profiles (partially corresponding to CVF and MSF) stand out as those highlighting the most unstable parts of the western flank of Mt. Vettore (Figure 1b and Figure 4). The surface fractures show a significant opening component (e.g. Figure 2d) at different locations along the s4-profile (Figure 5b, Figure 5e, and Tables S1-S2) and along the s2-profile (Figure 6b and Table S4), indicating significant slope instability-driven motion. These fractures were measured along the contact between the carbonates and the continental deposits (roughly corresponding to the trace of the structural elements, CVF and MSF), which we suspected in some cases corresponded to the crown of major landslides. In this area, the gravity-induced displacements are mainly driven by shear strain, explaining the predominant vertical component of the observed sliding and the VR to HR ratio generally >1.

The influence of gravity-driven displacements is also highlighted by the good fit between the direction of motion observed in the field (assumed to be roughly coincident with the dip direction of fractures) and the down slope direction of gravity-induced movement, parallel to the direction of maximum slope (aspect value). Such a positive correlation does not occur along the upper section of southern MSF (reported as s3-profile in Figure S2), where other processes than gravity influence the dip direction. In a recent paper, Iezzi et al. (2018) stated that slip vector angles measured along the CVF fall in the N210°–N270° range. From this observation they inferred, without reporting any quantitative misfit, that the slip vector angles are not correlated with the maximum slope orientation (aspect value; calculated from a 10 m DEM by Tarquini et al. (2002)), thus ruling out the possibility of any gravity-driven movement. Interestingly enough, the aspect value that we calculate from the same DEM is essentially in the same range of the dip direction reported in the database along the fracture zones of Mt. Vettore (Figure 7, Figure S5 and Table 2). For the CVF, specifically investigated by Iezzi et al. (2018), our analysis for the entire fracture zone results in an angular discrepancy of 10.3° and 18.2° between the aspect and fracture dip direction of each database entry, respectively for the Amatrice and Norcia earthquakes. We also find a good correspondence between the few slip vector angles (Figure 7) measured at selected sites at the contact limestone/SDCE materials (Perouse et al., 2018) and the maximum slope orientation. Perouse et al. (2018) attributed the displacement entirely to primary faulting with oblique kinematics, inferring a change from oblique dextral to pure normal to oblique sinistral slip along the concave fracture zone at mid-slope (Figure 2a and Figure 2l). Slip vector angles reported by Perouse et al. (2018), however, are compatible with the direction of maximum slope (Figure 7). Thus, an influence of the gravity, eventually mixed with primary faulting, on reported displacements cannot be excluded. More, in the crown of the sliding bodies

shown in Figure 2h and Figure 2l, the fractures are oriented perpendicular to the main slope, while along the flanks of the same sliding bodies they are arranged in an en-echelon pattern. The continuity of the fractures and the pattern delineated by their orientation recall the typical feature of gravitational sliding, bounded in the crown by arcuate fractures striking parallel to the slope and by dextral and sinistral en-echelon fractures cutting the slope along the right and left flanks, respectively (Varnes, 1978, Keefer, 1984; Cotton et al. 1990).

The evidence for gravitational displacement supplied by the arcuate and downslope concave fracture pattern (Figure 2h and Figure 2l) is even more evident at the smaller scale of each individual fracture and in loose continental deposits (SDCE). In these deposits, the orientation of the fractures is often similar to that of pre-existing geologic structures (e.g. bedrock fault scarps), but at local scale they preserve a concave-up shape. The gravitational features identified by our geomorphological interpretation and with previous investigations of the area (Giovagnotti, 1979; Coltorti & Farabollini, 1995, Aringoli et al., 2010) favored the development and the spatial arrangement of fractures.

The only area of the deformation zone that is unaffected by significant secondary-coseismic effects is the fracture zone in the Piano Grande, at the foothills of the western flank of Mt. Vettore (Figure 1b and Figure 8a). Following the Amatrice earthquake, these fractures appeared sporadic, discontinuous, and were characterized by low VR and HR values. Spatially, they approximately correspond to the zone where Galadini & Galli, 2003 found paleoseismological evidence for past coseismic ruptures. Following the Norcia earthquake, this fracture zone gained a well-expressed, linear to curvilinear spatial continuity with an average NNW-SSE trend. Unlike the slopes of Mt. Vettore, this fracture zone did not develop at the contact between different lithological units at the surface. Furthermore, the local morphology, though heavily modified by centuries of agricultural activity, is characterized by a negligible slope gradient (less than 3°; see Figure 4). We may conclude that the coseismic deformation in the Piano Grande was not affected by either gravity-driven mechanism or rheological differences, and hence is a good candidate for true surface faulting; whether it represents primary faulting, or rather the upward propagation of a secondary splay is outside the scope of this study.

7. Conclusions

With this contribution we intended to raise awareness of the role that the topography and the rheology of the outcropping lithologies may play in a mountainous zone under seismic loading.

The assumption that any coseismic deformation of the topographic surface has to be attributed entirely to tectonic faulting prevents a full understanding of the role played by other important morphogenic processes, including lateral variations of rheological properties, gravitational movements and soil densification.

We analyzed the effects of the 2016 central Italy earthquake sequence with an integrated geological, structural, and geomorphological approach combined with numerical modeling of earthquake-induced deformation. Notwithstanding the uncertainties involved in the definition of all relevant modeling parameters, this procedure allowed us to provide firm constraints on the role played by gravity-driven processes.

Our analysis suggests that rheology and gravity-driven displacements can never be dismissed as marginal in any high topography region, and especially in areas that have experienced slope instabilities in the past. We show (a) that gravity-driven mass movements

occurred repeatedly along the western flank of Mt. Vettore well before the 2016 earthquakes, and (b) that the distribution of coseismic fractures following the Amatrice and Norcia earthquakes is spatially well correlated with the previously identified mass movement features.

Thus, we conclude that along steep slopes, the exposure of fault planes and the generation of fractures in unconsolidated sediments is due to the continuous interaction of structural and geomorphologic elements with gravitational and erosion-depositional processes. So far this interaction is often overlooked, but is proven here to be significant and in many instances even dominant, as recently documented by Kastelic et al. (2017) for a number of "nastrini di faglia" ("fault ribbons") of the central Apennines.

Conversely, when fracture zones develop either in flat areas, or in the absence of significant rheological contrasts, such as in the Piano Grande Plain, coseismic surface ruptures can reasonably be assigned a true tectonic origin.

Our result underline that when investigating active tectonics and surface faulting in a mountainous area, any surface deformation processes need to be investigated from different perspectives, possibly merging diverse expertise into a single team. By doing this, the global earthquake geology community could prevent both field geologists and modelers from overweighting the tectonic component of surface deformation, thus inevitably introducing a bias in the resulting interpretations and inferences.

In summary, the earthquake geology community must take full advantage of well investigated earthquakes such as the Amatrice and Norcia events. These cases offer good quality instrumental evidence that should be employed in establishing the modes and the rules by which coseismic slip at seismogenic depth is transferred to the surface. The correctness of such rules is a fundamental prerequisite for properly assessing the magnitude of large earthquakes of the past and the slip rate of their causative faults, and ultimately for supplying the most reliable information to seismic hazard practitioners.

Acknowledgments, Samples, and Data

This study has benefited from funding provided by project MIUR-FIRB “Abruzzo” (codes RBAP10ZC8K_001, RBAP10ZC8K_003 and RBAP10ZC8K_007), L.R. Abruzzo n.37/2016 (“Indagini di geologia, sismologia e geodesia per la mitigazione del rischio sismico”), RECAPTIVE (Bottom Up FISR 2016) and by the Italian Presidenza del Consiglio dei Ministri –Department of Civil Protection (Accordo Quadro DPC-INGV, 2012-2021). Scientific papers funded by DPC do not represent its official opinion and policies. Part of the research was carried out at the Jet Propulsion Laboratory, California Institute of Technology, under a contract with the National Aeronautics and Space Administration. We are grateful to Corpo Nazionale Soccorso Alpino e Speleologico (Mountain Rescue) for the logistic support and to G. Di Giulio for his valuable advice in the strong motion data analysis. We acknowledge Emergeo WG for providing us with coseismic fracture database (published in Emergeo WG, 2016). The original coseismic fracture database for the Norcia-earthquake and the strong motion data can be retrieved from Villani et al. (2018) and Luzi et al. (2018), respectively. The panchromatic orthophotos used in the photo-interpretation are retrieved from https://www.pcn.minambiente.it/mattm/servizio-wms/. The Scoops and Slammer software used in the slope stability analysis can be downloaded at https://www.ssap.eu/downloads.html and from the USGS at https://pubs.usgs.gov/tm/12b1/, respectively. The coseismic fracture data point resulting by our analysis is in the Supplementary Material: Table S1 to S6. The authors acknowledge comments from Associate Editor Mikael Attal and three Anonymous Reviewers that helped to add clarity of the presented research and generally improved the manuscript. Discussions and feedbacks from G. Valensise increased the overall quality of this paper.

References

Albano, M., Saroli, M., Moro, M., Falcucci, E., Gori, S., Stramondo, S., et al. (2016). Minor shallow gravitational com-ponent on the Mt. Vettore surface ruptures related to MW 6, 2016 Amatrice earthquake. *Annals of Geophysics*, 59, Fast Track 5. Doi: 10.4401/ag-7229

AMA_LOC Working Group (2016a). Amatrice 2016 main events re-location (v1.0 – 20160902 12.00). Istituto Nazionale di Geofisica e Vulcanologia. Doi: 10.5281/zenodo.61371

AMA_LOC Working Group (2016b). AMATRICE 2016 aftershocks re-location catalogue (v1.0 – from 20160824 01:41 to 20160831 12:19). Doi: 10.5281/zenodo.61404

Arfken, G.B., & Weber, H.J. (1995). *Mathematical Methods for Physicists*. (4th edition). New York Academic Press.

Aringoli, D., Cavitolo, P., Farabollini, P., Galindo-Zaldivar, J., Gentili, B., Giano, S.I., Lòpez-Garrido, A.C., Materazzi, M., Nibbi, L., Pedrera, A., Pambianchi, G., Ruano, P., Ruiz-Constàn, A., Sanz de Galdeano, C., Savelli, D., Tondi, E., Troiani, F. (2014). Morphotectonic characterization of the quaternary intermontane basins in the Umbria-Marche Apennines (Italy). *Rendiconti Lincei*, 25/2, 11-128.

Aringoli, D., Gentili, B., Materazzi, M., & Pambianchi, G. (2010). Mass movements in Adriatic Central Italy: activation and evolutive control factors. In E. Werner et al. (Eds.), *Landsclides: Causes, types and effects* (pp. 1-71). Nova Science Puplisher, Inc. ISBN: 978-1-60741-258-8.

Bianchi Fasani, G., Di Luzio, E., Esposito, C., Evans, S. G., & Scarascia Mugnozza, G. (2014). Quaternary, catastrophic rock avalanches in the Central Apennines (Italy): Relationships with inherited tectonic features, gravity-driven deformations and the geodynamic frame. *Geomorphology*, 211, 22-42. http://dx.doi.org/10.1016/j.geomorph.2013.12.027

Boncio, P., Lavecchia, G., Milana, G., & Rozzi, B. (2004). Seismogenesis in Central Apennines, Italy: an integrated analysis of minor earthquake sequences and structural data in the Amatrice-Campotosto area. *Annals of Geophysics*, 47(6), 1723-1742. Doi: 10.4401/ag-3371

Bonini, L., Maesano, E. M., Basili, R., Burrato, P., Carafa, M. M. C., Fracassi, U., et al. (2016). Imaging the tectonic framework of the 24 August 2016, Amatrice (central Italy) earthquake sequence: new roles for old players?. *Annals of Geophysics*, 59, Fast Track 5. Doi: 10.4401/ag-7229

Borselli, L. (2018). SSAP 4.9.6 – Slope Stability Analysis Program. Manuale di riferimento del codice SSAP Versione 4.9.6. Retrived from http://www.ssap.eu/manualessap2010.pdf (last accessed 05 May 2018).

Brozzetti, F., & Lavecchia, G. (1994). Seismicity and related extensional stress field: The case of the Norcia seismic zone (central Italy). *Annales Tectonicae*, 8, 36–57.

Calamita, F., Pizzi, A., & Roscioni, M. (1992). I fasci di faglie recenti ed attive di M. Vettore-M. Bove e di Castello-M. Cardosa (Appennino Umbro-Marchigiano). *Studi Geologici Camerti*, 1992/I, 81-95.

Carafa, M. M. C., & Bird, P. (2016). Improving deformation models by discounting transient signals in geodetic data: 2. Geodetic data, stress directions, and long-term strain rates in Italy. *Journal of Geophysical Research: Solid Earth*, 121(7), 5557-5575. Doi: 10.1002/2016JB013038

Carta Geologica Regionale 1:10000 – Regione Umbria (2016). Geoportale WebGis Regione Umbria. Direzione Ambiente, Territorio e Infrastrutture Servizio Geologico e Sismico. Retrieved from http://storicizzati.territorio.regione.umbria.it/Static/GeologiaKmz/GeologiaKmz/Index_kmz.htm. (last accessed 9 May 2018)

Chen, T. C., Lin, M. L., & Hung, J. (2004). Pseudostatic analysis of Tsao-Ling rockslide caused by Chi-Chi earthquake. *Engineering Geology*. 71(1-2), 31-47. https://doi.org/10.1016/S0013-7952(03)00124-8

Chen, X. L., Ran, H. L., & Yang, W. T. (2012). Evaluation of factors controlling large earthquake-induced landslides by the Wenchuan earthquake. *Natural Hazard and Earth System Sciences*, 12, 3645-3657. https://doi.org/10.5194/nhess-12-3645-2012

Chiaraluce, L., Di Stefano, R., Tinti, E., Scognamiglio, L., Michele, M., Casarotti, E., et al. (2017). The 2016 Central Italy Seismic Sequence: A First Look at the Mainshocks, Aftershocks, and Source Models. *Seismological Research Letters*, 88(3), 757-771. https://doi.org/10.1785/0220160221

Chowdhury, R., Flentje, P., & Bhattacharya, G. (Eds.) (2009). *Geotechnical Slope Analysis*. CRC Press, The Netherlands. ISBN 978-0-415-46974-6.

Coltorti, M., & Farabollini, P. (1995). Quaternary evolution of the "Castelluccio di Norcia" basin (Umbro-Marchean Apennines, Central Italy). *Il Quaternario*, 8(1), 149-166.

Cotton, W. R., Fowler, W. L., & Van Velsor, J. E. (1990). Coseismic bedding plane faults and ground fissures associated with the Loma Prieta earthquake of 17 October 1989. In S. R. McNutt & R. H. Sydnor (Eds.), *The Loma Prieta (Santa Cruz Mountains), California, earthquake of 17 October 1989* (Special Publication, Vol. 104, pp. 95-104). Sacramento, CA, Division of Mines and Geology.

D'Agostino, N., Jackson, J. A., Dramis, F., & Funiciello, R. (2001). Interactions between mantle upwelling, drainage evolution and active normal faulting: an example from the central Apennines (Italy). *Geophysical Journal International*, 147(2), 475-497. https://doi.org/10.1046/j.1365-246X.2001.00539.x

Demangeot, J. (1973). Néotectonique et dépõts quaternaires dans l'Apennin. *Acc. Naz. Lincei, anno CCCLXX*, 215-240.

Di Luzio, E., Bianchi Fasani, G., Esposito, C., Saroli, M., Cavinato, G. P., & Scarascia Mugnozza, G. (2004). Massive rock-slope failure in the Central Apennines (Italy): the case of the Campo di Giove rock avalanche. *Bulletin of Engineering Geology and the Environment*, 63(1), 1-12, http://dx.doi.org/10.1007/s10064-003-0212-7

Duncan, J. M. (1996). State of the art: Limit equilibrium and finite-element analysis of slopes. *Journal of Geotechnical Engineering*, 122(7), 577-596. https://doi.org/10.1061/(ASCE)0733-9410(1996)122:7(577)

Emergeo Working Group (2016). Coseismic effects of the 2016 Amatrice seismic sequence: first geological results. *Annals of Geophysics*, 59, Fast Track 5. Doi: 10.4401/ag-7195

Emergeo Working Group (2017a). Photographic collection of the coseismic geological effects originated by the 24th August 2016, Amatrice (Central Italy) seismic sequence. *Miscellanea INGV*, 34, 1-114. Retrived from http://www.ingv.it/editoria/miscellanea/2017/miscellanea34/.

Emergeo Working Group (2017b). A new photographic dataset of the coseismic geological effects originated by the Mw5.9 Visso and Mw6.5 Norcia earthquakes (26th and 30th

October 2016, Central Italy). *Miscellanea INGV*, 38, 1-114. Retrived from http://www.ingv.it/editoria/miscellanea/2017/miscellanea38/

EN 1998-1 (2004). Eurocode 8: Design of structures for earthquake resistance. Part 1: general rules, seismic actions and rules for buildings. CEN European Committee for Standardization. Bruxelles, Belgium.

Esposito, C., Bianchi Fasani, G., Martino, S., & Scarascia Mugnozza, G. (2013). Quaternary gravitational morpho-genesis of Central Apennines (Italy): Insights from the Mt. Genzana case history. *Tectonophysics*, 605, 96-103. http://dx.doi.org/10.1016/j.tecto.2013.06.023

Esposito, E., Martino, S., & Scarascia Mugnozza, G. (2007). Mountain slope deformations along thrust fronts in jointed limestone: an equivalent continuum modelling approach. *Geomorphology*, 90, 55-72. Doi:10.1016/j.geomorph.2007.01.017

Fortunato, C., Martino, S., Prestininzi, A., Romeo, R.W., coauthors Fantini A., Sanandrea P. (2012). New release of the Italian catalogue of earthquake-induced ground failures (CEDIT). *Italian Journal of Engineering Geology and Environment*. Doi: 10.4408/IJEGE.2012-02.O-05

Franke, K., Kayen, R. E., Lingwall, B. L., Tommasi P., della Pasqua F., Zimmaro P., et al. (2017). Slope displacements, landslides, and rockfalls. In P. Zimmaro & J. P Stewart (Eds.), *Engineering Reconnaissance following the October 2016 Central Italy earthquakes Version 2*, (Report, chapter 4, pp.1-76). Doi:10.18118/G6HS39.

Galadini, F. (2006). Quaternary tectonics and large-scale gravitational deformations with evidence of rock-slide displacements in the Central Apennines (central Italy). *Geomorphology*, 82(3-4), 201-228. Doi: 10.1016/j.geomorph.2006.05.003

Galadini, F., & Galli, P. (2000). Active tectonics in the central Apennines (Italy) - Input data for seismic hazard assessment. *Natural Hazards*, 22(3), 225-270. Doi: 10.1023/A:1008149531980

Galadini, F., & Galli, P. (2003). Paleoseismology of silent faults in the central Apennines (Italy): the Mt. Vettore and Laga Mts. Faults. *Annals of Geophysics*, 46(5), 815-836. Doi: 10.4401/ag-3457

Gentili, B., & Pambianchi, G. (1989). Morfogenesi fluviale ed attività antropica nelle Marche centro-meridionali. *Geografia Fisica e Dinamica Quaternaria*, 10, 204-217.

Giovagnotti, C. (1979). Lineamenti paleogeografici e geomorfologici dei Monti Sibillini. *Lavori della Società Italiana di Biogeografia*, 6, 29-79.

Gispert Busquets, S. (2016). Remote sensing aerial and satellite-based mapping of earthquake-induced landslides: 2016 The Amatrice earthquake (II Level Master's thesis). University of Ceri-La Sapienza, Roma, Italy.

Gruppo di lavoro IREA-CNR & INGV (2016). Sequenza sismica di Amatrice: Aggiornamento delle analisi interferometriche satellitari e modelli di sorgente. https://doi.org/10.5281/zenodo.61682

Guidoboni, E., Ferrari, G., Mariotti, D., Comastri, A., Tarabusi, G., Sgattoni, G., & Valensise, G. (2018). CFTI5Med, Catalogo dei Forti Terremoti in Italia (461 a.C.-1997) e nell'area Mediterranea (760 a.C.-1500). Istituto Nazionale di Geofisica e Vulcanologia (INGV). Retrived from http://storing.ingv.it/cfti/cfti5/(last accessed 3 May 2018)

Hoek, E., & Brown, E.T. (1997). Practical estimates of rock mass strength. *International Journal of Rock Mechanics and Mining Sciences*, 34(8), 1165-1186.

Hoek, E., & Marinos, P. (2000). Predicting Tunnel Squeezing problems in weak heterogeneous rock masses. *Tunnels and Tunnelling International*, 32(11-12), 45–51 and 34–36.

Hoek, E., Carranza Torres, C. T., & Corkum, B. (2002). *Hoek-Brown failure criterion – 2002 Edition*. Proceading presented at the North American Rock Mechanics Society meeting (1, pp. 267-273), Toronto, Canada.

Hoek, E., Marinos, P. & Benissi, M. (1998). Applicability of the Geological Strength Index (GSI) classification for very weak and sheared rock masses. The case of the Athens Schist Formation. *Bullettin of Engineering Geology and the Environment*, 57(2), 151-160.

Huang, M. H., Fielding, E. J., Liang, C., Milillo, P., Bekaert, D., Dreger, D., & Salzer, J. (2017). Coseismic deformation and triggered landslides of the 2016 Mw 6.2 Amatrice earthquake in Italy. *Geophysical Research Letters*, 44(3), 1266-1274. https://doi.org/10.1002/2016GL071687

Iezzi, F., Mildon, Z., Walker, J. F., Roberts, G., Goodall, H., Wilkinson, M., & Robertson, J. (2018). Coseismic throw variation across along- strike bends on active normal faults: implications for displacement versus length scaling of earthquake ruptures. *Journal of Geophysical Research: Solid Earth*, 123. https://doi.org/10.1029/2018JB016732

Janbu, N. (1973). Slope stability computations. In R. C. Hirschfield and S. J. Poulos (Eds.), *The embankment dam Engineering Casagrande Volume* (pp. 47-86). New York, USA, John Wiley and Sons.

Jibson, N. (1993). Predicting Earthquake induced landslides displacements using Newmark's sliding block analysis. *Transportation Research Record* (Vol. 1441, pp. 9-17). Washington D.C., TRB: National Research council. ISSN: 0361-1981

Jibson, R. W. (2011). Methods for assessing the stability of slopes during earthquakes-A retrospective. *Engineering Geology*, 122(1-2), 43-50. Doi: 10.1016/j.enggeo.2010.09.017

Jibson, R. W., Rathje, E. M., Jibson, M. W., & Lee, Y. W. (2013). SLAMMER—Seismic LAndslide Movement Modeled using Earthquake Records (ver.1.1, November 2014). *Techniques and Methods* (Technical Report, book 12, chapter B1, unpaged). Reston, VA, U.S. Geological Survey.

Kastelic, V., Burrato, P., Carafa, M. M. C., & Basili, R. (2017). Repeated surveys reveal nontectonic exposure of supposedly active normal faults in the central Apennines, Italy. *Journal of Geophysical Research: Earth Surface*, 122, 114-129. Doi:10.1002/2016JF003953

Keefer, D. K. (1984). Landslides caused by earthquake. *Geological Society of America Bulletin*, 95(4), 406–421. https://doi.org/10.1130/0016-7606(1984)95<406:LCBE>2.0.CO;2

Keefer, D. K. (2000). Statistical analysis of an earthquake-induced landslide distribution — the 1989 Loma Prieta, California event. *Engineering Geology*, 58(3-4), 231-249. Doi: 10.1016/S0013-7952(00)00037-5

Khazai, B., & Sitar, N. (2004). Evaluation of factors controlling earthquake-induced landslides caused by Chi-Chi earthquake and comparison with the Northridge and Loma Prieta events. *Engineering Geology*, 71(1-2), 79-95. https://doi.org/10.1016/S0013-7952(03)00127-3

Krahn, J. (2003). The 2001 R.M. Hardy lecture: the limits of limit equilibrium analysis. *Canadian Geotechnical Journal*, 40, 643–660. Doi: 10.1139/T03-024

Lavecchia, G., Brozzetti, F., Barchi, M., Menichetti, M., & Keller, J. V. A. (1994). Seismotectonic Zoning in East-Central Italy Deduced from an Analysis of the Neogene to Present Deformations and Related Stress-Fields. *Geological Society of America Bulletin*, 106(9), 1107-1120. Doi: 10.1130/0016-7606(1994)106<1107:SZIECI>2.3.Co;2

Lavecchia, G., Castaldo, R., de Nadis, R., De Novellis, V., Ferrarini, F., Pepe, S., et al. (2016). Ground deformation and source geometry of the 24 August 2016 Amatrice earthquake (Central Italy) investigated through analytical and numerical modeling of DInSAR measurements and structural-geological data. *Geophysical Research Letters*, 43(24). Doi: 10.1002/2016GL071723

Luzi, L., Puglia, R., Russo, E., & ORFEUS WG5 (2016). Engineering Strong Motion Database, version 1.0. Istituto Nazionale di Geofisica e Vulcanologia, Observatories & Research Facilities for European Seismology. Doi: 10.13127/ESM

McCalpin, J. (Ed.). (2009). *Paleoseismology* (2nd ed.), San Diego, USA: Academic Press, Elsevier Publishing.

Michele, M., Di Stefano, R., Chiaraluce, L., Cattaneo, M., De Gori, P., Monachesi, G., et al. (2016). The Amatrice 2016 seismic sequence: a preliminary look at the mainshock and aftershocks distribution. *Annals of Geophysics*, 59, Fast Track 5. Doi: 10.4401/ag-7227

Newmark, N.M. (1965). Effects of earthquakes on dams and embankments. *Geotechnique*, 15 (2), 139-160. https://doi.org/10.1680/geot.1965.15.2.139

Patacca, E., Sartori, R., & Scandone, P. (1990). Tyrrhenian basin and Apenninic arcs: kinematic relations since Late Tortonian times. *Memorie della Società Geologica Italiana*, 45, 425-451.

Perouse, E., Benedetti, L., Fleury, J., Rizza, M., Puliti, I., Billant, J., Van der Woerd, J., Feuillet, N., Jacques, E., & Pace, B. (2018). Coseismic slip vectors of August 24 and October 30 2016 earthquakes in central Italy: oblique slip and regional kinematic implications. *Tectonics*, 37. https://doi.org/10.1029/2018TC005083doi: 10.1029/2018TC005083

Piacentini, T., Miccadei, E. (2014). The role of drainage systems and intermontane basins in the Quaternary landscape of the Central Apennines chain (Italy). *Rendiconti Lincei*, 25/2, 139-150. https://doi.org/10.1007/s12210-014-0312-2

Pierantoni, P. P., Deiana, G., & Galdenzi, S. (2013). Geological map of the Sibillini Mountains (Umbria-Marche Apennines, Italy). *Italian Journal of Geoscience (Boll. Soc. Geol. It.)*, 132(3), 497-520. Doi: 10.3301/IJG.2013.08

Pizzi, A., & Galadini, F. (2009). Pre-existing cross-structures and active fault segmentation in the northern-central Apennines (Italy). *Tectonophysics*, 476(1-2), 304-319. Doi: 10.1016/j.tecto.2009.03.018

Pizzi, A., Di Domenica, A., Gallovic, F., Luzi, L., & Puglia, R. (2017). Fault Segmentation as Constraint to the Occurrence of the Main Shocks of the 2016 Central Italy Seismic Sequence. *Tectonics*, 36(11), 2370-2387. https://doi.org/10.1002/2017TC004652

Polcari, M., Montuori, A., Bignami, C., Moro, M., Stramondo, S., & Tolomei, C. (2017). Using multi-band InSAR data for detecting local deformation phenomena induced by the 2016–2017 Central Italy seismic sequence. *Remote Sensing of Environment*, 201, 234-242. https://doi.org/10.1016/j.rse.2017.09.009

Pradel, D., Smith, P. M., Steward, J. P., & Raad, G. (2005). Case History of Landslide Movement during the Northridge Earthquake. *Journal of Geotechnical and Geoenvironmental Engineering*, 131(11), 1360-1369. https://doi.org/10.1061/(ASCE)1090-0241(2005)131:11(1360)

Roback, K., Clark, M. K., West, A. J., Zekkos, D., Li, G., Gallen, S. F., et al. (2018). The size, distribution, and mobility of landslides caused by the 2015 M(w)7.8 Gorkha earthquake, Nepal. *Geomorphology*, 301, 121-138. http://dx.doi.org/10.1016/j.geomorph.2017.01.030

Rogers, J. D., & Chung, J. W. (2016). Applying Terzaghi's method of slope characterization to the recognition of Holocene land slippage. *Geomorphology*, 265, 24-44. http://dx.doi.org/10.1016/j.geomorph.2016.04.020

Romeo, R. (2000). Seismically induced landslide displacements: a predictive model. *Engineering Geology*, 58, 337–351.

Salisbury, J.B., Haddad, D.E., Rockwell, T., Arrowsmith, J R., Madugo, C., Zielke, O., & Scharer, K., 2015, Validation of meter-scale surface faulting offset measurements from high-resolution topographic data. *Geosphere*, 11(6), 1884–1901. Doi:10.1130 /GES01197.1.

Servizio Geologico d'Italia (1941). *Geological Map of Italy* (Sheet 132 ,Norcia, scale 1:100,000). Istituto Poligrafico e Zecca dello Stato, Roma.

Tarquini, S., Vinci, S., Favalli, M., Doumaz, F., Fornaciai, A., and Nannipieri, L., (2012). Release of a 10-m-resolution DEM for the Italian territory: Comparison with global-coverage DEMs and anaglyph-mode exploration via the web. *Computers & geosciences*, 38(1), 168-170.

Trigila, A., Iadanza, C., & Spizzichino, D. (2010). Quality assessment of the Italian Landslide Inventory using GIS processing. *Landslides*: *Journal of the International Consortium on Landslides*, 7(4), 455-470. Doi: 10.1007/s10346-010-0213-0

Valensise, G., Vannoli, P., Basili, R., Bonini, L., Burrato, P., Carafa, M. M. C., et al. (2016). Fossil landscapes and youthful seismogenic sources in the central Apennines: excerpts from the 24 August 2016, Amatrice earthquake and seismic hazard implications. *Annals of Geophysics*, 59, Fast Track 5. Doi: 10.4401/ag-7215

Varnes, D. J. (1978). Slope movement types and processes. In R. L. Schuster & R. J., Krizek (Eds.), *Landslides: Analysis and control* (Special Report, 176, pp. 11-33). Washington D.C, Transportation and Road Research Board, National Academy of Science.

Villani, F.,et al. (2018). A database of the coseismic effects following the 30 October 2016 Norcia earthquake in Central Italy. *Scientific Data*, 5, 180049. doi: 10.1038/sdata.2018.49

Wang, J. A., Yao, L. K., & Hussain, A. (2010). Analysis of earthquake-triggered failure mechanisms of slopes and sliding surfaces. *Journal of Mountain Science*, 7(3), 282-290. Doi: 10.1007/s11629-010-2020-4

Wilkinson, M. W., McCaffrey, K. J. W., Jones, R. R., Roberts, G. P., Holdsworth, R. E., Gregory, L. C., et al. (2017). Near-field fault slip of the 2016 Vettore Mw 6.6 earthquake (Central Italy) measured using low-cost GNSS. *Scientific Report*, 7(1), 4612. Doi: 10.1038/s41598-017-04917-w

Xu, C., Xu, X. W., & Shyu, J. B. H. (2015). Database and spatial distribution of landslides triggered by the Lushan, China Mw 6.6 earthquake of 20 April 2013. *Geomorphology*, 248, 77-92. http://dx.doi.org/10.1016/j.geomorph.2015.07.002

Table 1

Rheological parameters for slope modeling

layer	c[a] (kPa)	φ[b] (°)	γ[c] (kN/m^3)		
1 (SDCE)	0-5	34-37	16-20		
	σ_{ci}[d] (kPa)	*GSI*[e]	γ[c] (kN/m^3)	m_i[f]	D[g]
2 (carbonates)	50-100	30-45	27	9±2	0

[a]Cohesion. [b]Angle of internal friction. [c]Unit weight volume. [d]Uniaxial compressive strength of the intact rock. [e]Geological Strength Index (Hoek et al., 1998; Hoek and Marinos, 2000). [f]Material constant. [g]Disturbance factor.

Table 2

Slope and Fracture Statistical Analysis

Pz-point	Fracture zone	DEM Aspect Maximum Slope Direction (°)			Fracture Analysis Amatrice				Fracture Analysis Norcia			
					N[c]	Dip Direction (°)			N[c]	Dip Direction (°)		
		(Min)	(Avg)	(Max)		(Min)	(Avg)	(Max)		(Min)	(Avg)	(Max)
P1	CVF[a]	249	**256**	262	105	207	**243**	279	45	193	**241**	268
P2	CVF[a]	253	**261**	273	107	187	**246**	311	18	119	**240**	279
P3	CVF[a]	229	**248**	257	115	187	**233**	276	30	48	**228**	278
P4	CVF[a]	217	**232**	244	175	147	**230**	284	46	35	**224**	285
P5	CVF[a]	212	**226**	238	126	172	**219**	278	37	25	**208**	242
P6	CVF[a]	216	**222**	234	128	168	**212**	260	59	22	**195**	353
P7	MSF[b]	250	**261**	269	/	/	**/**	/	40	230	**265**	305
P8	MSF[b]	247	**255**	263	/	/	**/**	/	25	233	**265**	308
P9	MSF[b]	245	**251**	260	2	213	**223**	283	59	95	**283**	327
P10	MSF[b]	237	**243**	246	23	175	**239**	283	65	93	**253**	315
P11	MSF[b]	226	**239**	265	/	/	**/**	/	201	40	**241**	306

Note.[a] Fractures roughly distributed along the Cordone del Vettore Fault (CVF). [b] Fractures partially distributed along the Middle Slope Fault (MSF). [c] Number of fracture measurements.

The maximum slope direction is computed from 10 m DEM (Tarquini et al., 2012) and referred from the geographic N. The dip direction of fractures is from the Emergeo WG database and published in Emergeo WG (2016) for the Amatrice earthquake; and they can be retrieved from Villani et al. (2018) for the Norcia earthquake. The data statistical analysis was computed around the Pz-points with a 200-m buffer (see Figure 7 for location).

Note a high data variability for fracture analysis due to a high scatter of dip direction measurements. The frequency distribution is centered around its average, with low scatter in the tail values (Figure S5).

Table 3

List of selected Seismic Stations

Code	Origin time – UTC (yyyy-mm-dd hh:mm:ss)	Magnitude (M_w)	Network	Latitude (°)	Longitude (°)	Distance[c] (km)	Fault position	Geological unit	Soil class[f]	Topographic class[f]
CLO	2016-10-30 06:40:17	6.5	IT[a]	42.8294	13.2060	4	HW[d]	carbonates	A[g]	T1[j]
CNE	2016-10-30 06:40:17	6.5	IT[a]	42.8944	13.1528	11.3	HW[d]	continental d.	C[i]	T1[j]
MM01	2016-10-30 06:40:17	6.5	IV[b]	42.8993	13.3268	10.1	FW[e]	turbiditic silicoclastic d.	A[g]	T1[j]
NOR	2016-10-30 06:40:17	6.5	IT[a]	42.7924	13.0924	13.8	HW[d]	continental d.	C[i]	T1[j]
NRC	2016-08-24 01:36:32 2016-10-30 06:40:17	6.0 6.5	IT[a]	42.7925	13.0965	13.5	HW[d]	continental d.	B[h]	T1[j]
RQT	2016-08-24 01:36:32	6.0	IT[a]	42.8131	13.3110	4.8	FW[e]	turbiditic silicoclastic d.	B[h]	T1[j]
T1244	2016-10-30 06:40:17	6.5	IV[b]	42.7570	13.2978	8.4	FW[e]	turbiditic silicoclastic d.	B[h]	T1[j]

Note. The strong motion data can be retrieved from Luzi et al. (2018).
[a]Italian Strong Motion Network-RAN. [b]Italian National Seismic Network-RSN. [c]Station distance refers to the Cima del Redentore summit (see Figure 1 for location). [d]Station located in the hanging wall of the causative fault. [e]Station located in the foowall of the causative fault. [f]Soil and Topography classes according to the EC8 (EN 1998-1, 2004). [g]Seismic bedrock. [h]Very dense or stiff deposits. [i]Dense or stiff deposits. [j]Flat surface or isolated slopes with average slope angle ≤15°.

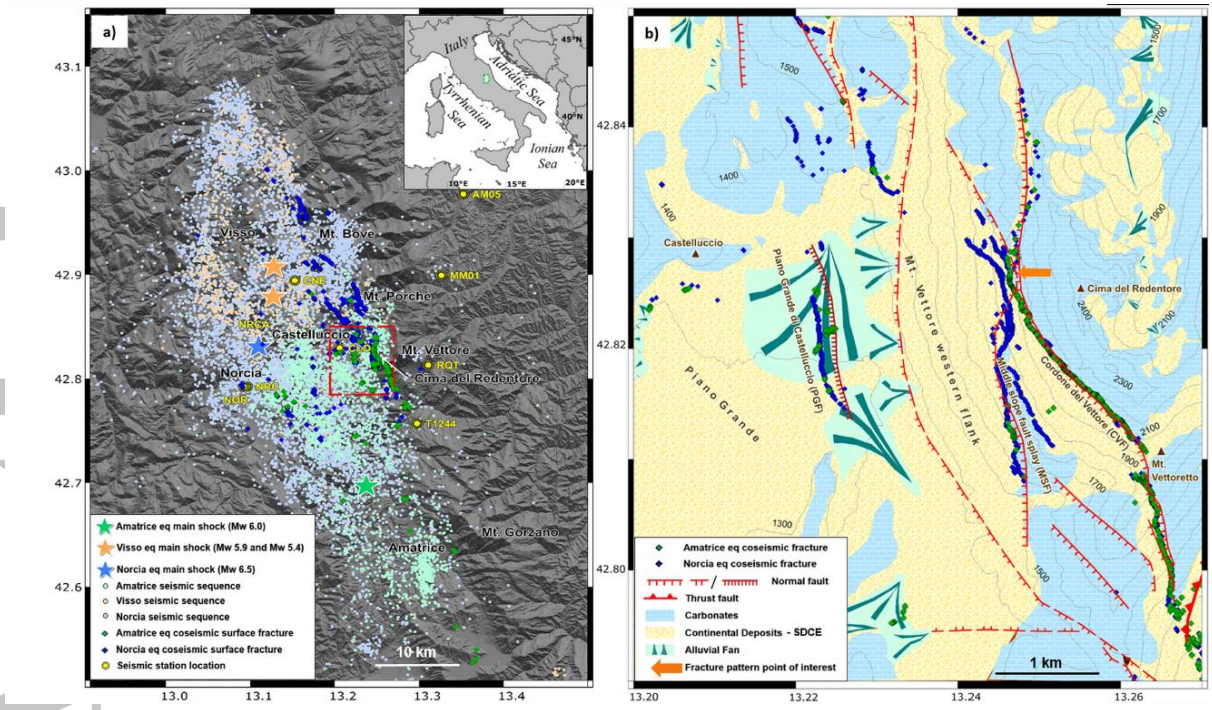

Figure 1. The 2016 central Italy earthquake sequence and its associated surface deformation along the western slopes of Mt. Vettore. (a) Location of the mainshocks and the spatial distribution of aftershocks (color-coded) for the three main earthquake sequences, along with the related surface deformation. The mainshock location and the aftershocks for the Amatrice sequence are from AMA_LOC Working Group (2016a and 2016b, respectively). Location of the Visso mainshock and of its aftershocks are from Michele et al., 2016. Location of the Norcia mainshock and of its aftershocks are from the INGV CNT FDSNWS event Web Service (accessible at http://webservices.rm.ingv.it/fdsnws/event/1/). The red dashed square presents the area depicted in Figure 1b. (b) Lithologic and structural characteristics of the Mt. Vettore area and distribution of surface fractures associated with Amatrice (green diamonds) and Norcia (blue diamonds) earthquakes. Data on lithology is taken from Pierantoni et al. (2013), integrated with our own field data. Structural data are from Pierantoni et al. (2013) (bright red continuous and discontinuous traces for normal and transtensive faults) and Galadini and Galli (2003) (dark red normal fault trace in the Piano Grande plain). The orange arrow points to the area where the fracture zone along the Cordone del Vettore fault (hereinafter CVF) is the most complex and closest to that developed along the second fault splay at middle slope of Mt. Vettore (hereinafter MSF) (see also the reference to this point of interest in the text).

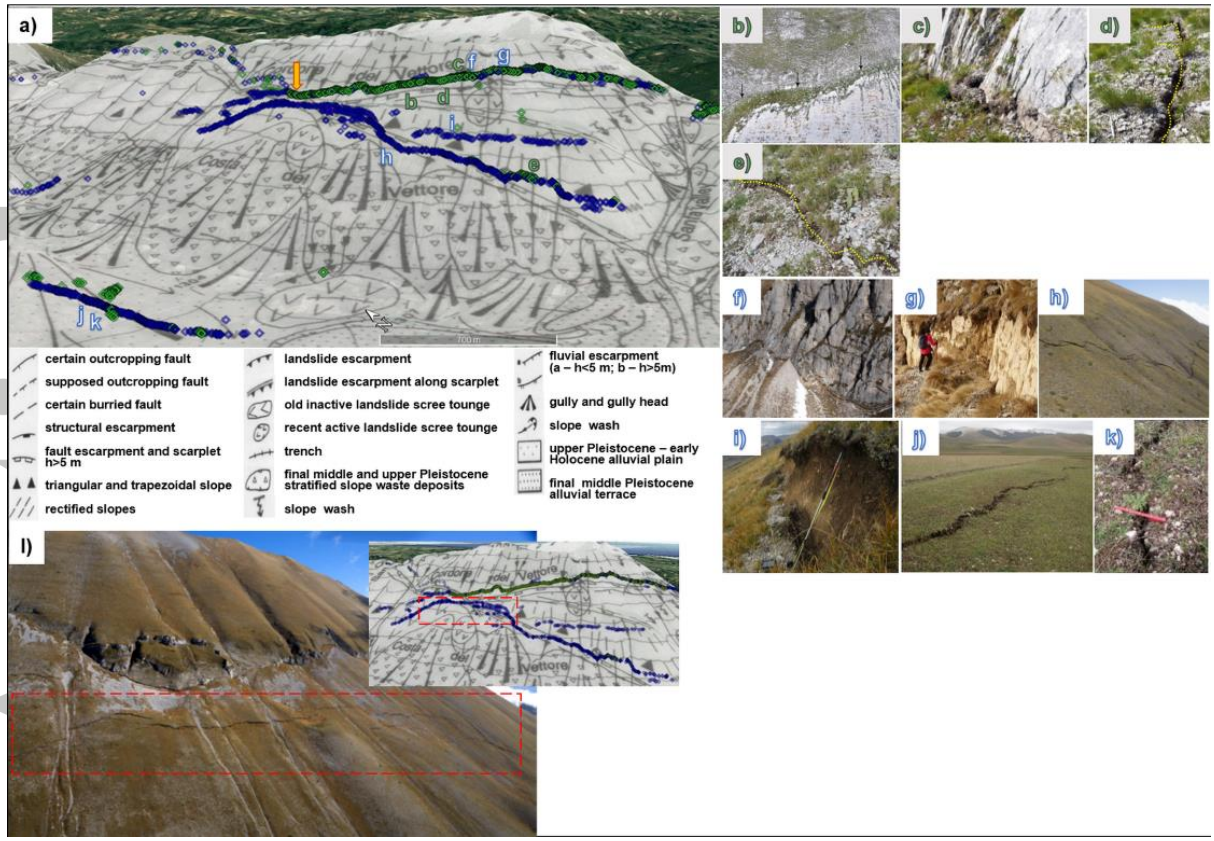

Figure 2. Characteristics of surface fractures along the western slope of Mt. Vettore. (a) Fracture distribution superimposed on the geomorphological map from Coltorti and Farabollini (1995), shown along with their original legend of the identified geomorphologic elements. The letters (b-k) correspond to the locations of the fractures shown on the right. The green (Amatrice) and blue (Norcia) diamond symbols are individual sampling sites (see also Figure 1b). As such, they do not represent continuous features but rather envelopes of small scale arcs (photos d and k). (b-e) Fractures observed after the Amatrice earthquake; unfortunately, there are no photos of the fractures in the Piano Grande fracture zone. Note the exposure of the bedrock scarp and the open, arcuate fractures (dotted yellow lines) in the Quaternary slope debris, colluvium-eluvium (hereinafter SDCE). (f-k) Fractures observed after the Norcia earthquake. Also in this case, we observed the additional bedrock scarp exposure as well as open fractures in the SDCE. Notice the fractures closely following the lithological contacts and their arrangement in arcuate shapes (f, h). (l) The fracture zone after the Norcia earthquake showing its concave downslope shape and the lateral shear zones that bound it on either side. The red squares in the main photo and in the inset represent roughly the same area interested by the concave fracture orientation. Photos b, c and, e are taken from Emergeo Working Group (2017a; photos n. 20, 32 and 34); photos f, h, i, and l are taken from Emergeo Working Group (2017b; photos n. 50, 52, 56 and 57); photo g is taken from Franke et al. (2017; Figure 2.14); photos d, j, and k are unpublished images taken by the authors. The scale of photos varies and covers several hundreds of meters (photos b, f, h), several meters (photos c, g, i, j) and several cm (up to 10 cm; photos d, e and k).

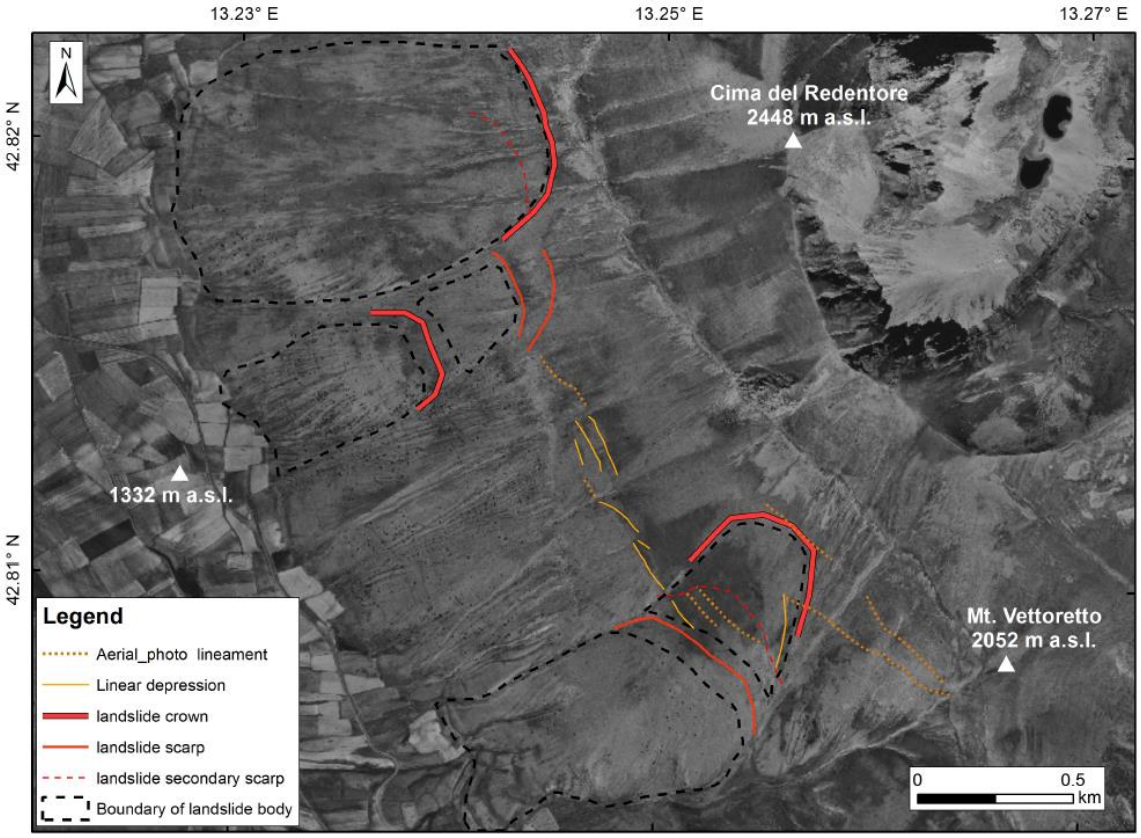

Figure 3. Gravity-driven linear landforms identified along the western slope of Mt. Vettore by interpretation of aerial photos, all taken before 2016 (1988, 1994 and 2000; the reader is referred to Figure S1 for the original photos). This panchromatic ortho-rectified photo is from 1994.

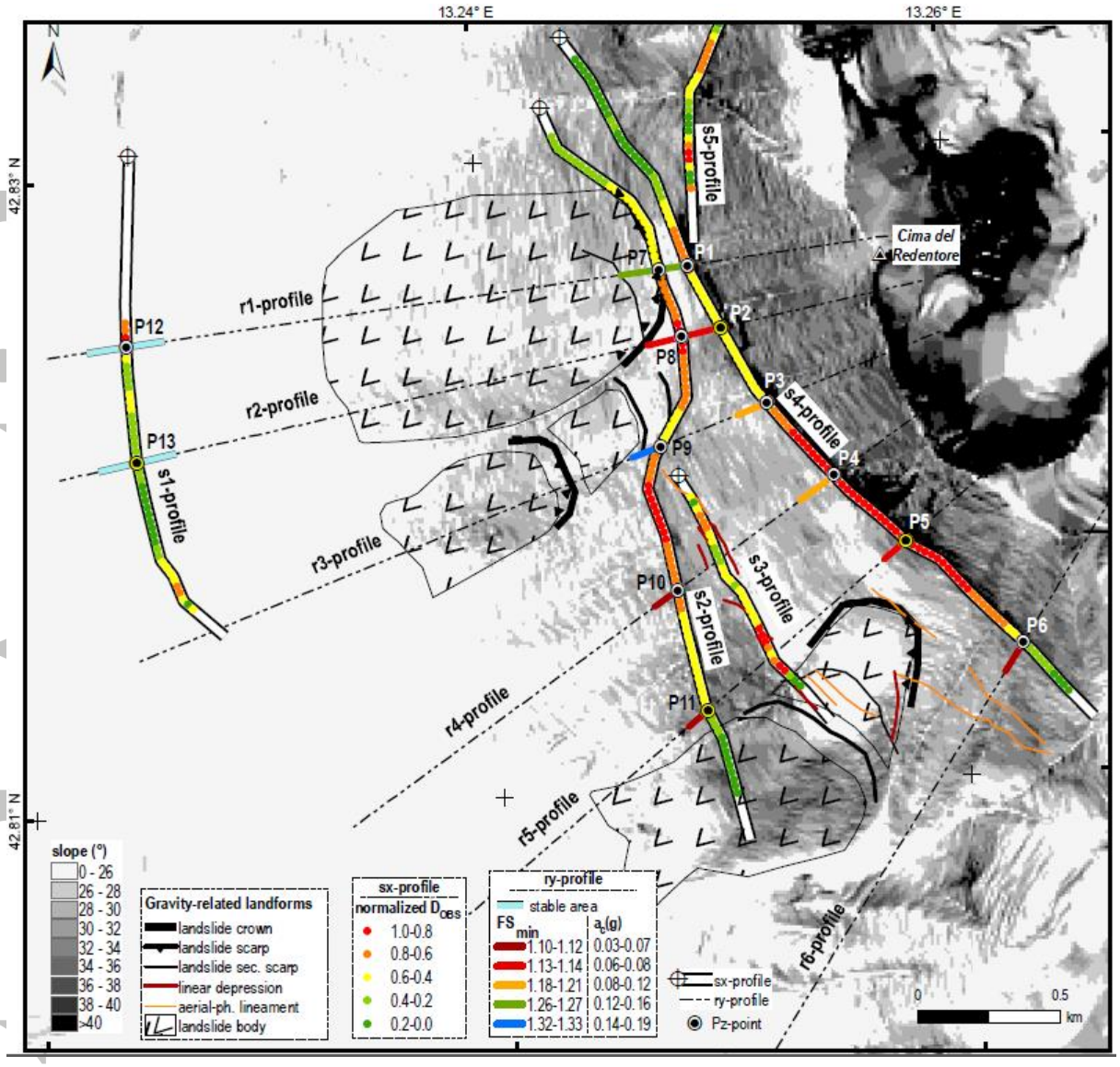

Figure 4. Total component of Norcia earthquake coseismic displacement (D_{OBS}) compared with the gravity-driven landforms, Factor of Safety (FS) and critical acceleration (a_c) computed in this study. The D_{OBS} points were fitted along the sx-profiles by the Chebyshev polynomials function and their values were normalized to the maximum value (~160 cm) fixed to 1 along the sx-profiles. The crossed circle at the northern tips of the sy-profiles represents the origin point of the abscises in Figures 5-6, Figure 11, Figure S3 and Figures S6-S7. The FS and a_c (see equation 2 and Section 5) were calculated along the ry-profiles with cohesion (c) equals to 0 and frictional angle (ϕ) equals to 33° along r1-, r2- r3- and r4-profiles, and ϕ equals to 35° along r5-, and r6-profiles (see Table 1 and Text S1 for details of geological models). The slope angle map was obtained from the 10 m DEM (Tarquini et al., 2012) and the gravity-driven landforms are from our photo-interpretation (Figure 3).

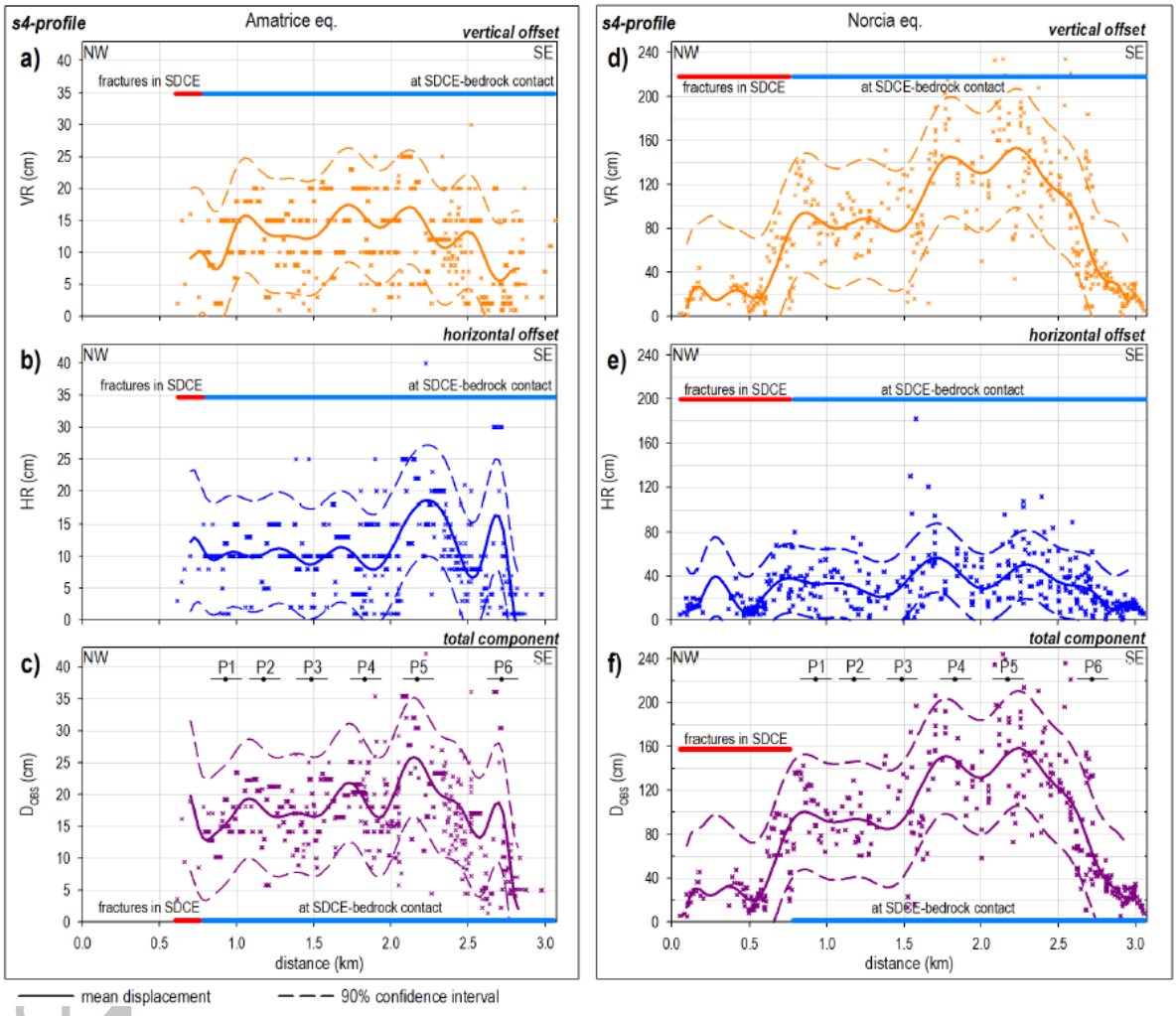

Figure 5. Plot of measured (crosses) and interpolated (lines) vertical (VR; a and d), horizontal (HR; b and e), and total offset (D_{OBS}; c and f) for the coseismic fractures along the s4-profile (see Figure 4 and Figure S2). The abscissa reports the distance in km from the northern tip of the s4-profile and its length depicts the final deformation zone, resulting from the cumulative effects of the Amatrice and Norcia earthquakes. Data were measured after the Amatrice (a, b and c) and the Norcia earthquakes (d, e and f), respectively. For the Amatrice earthquake the measured VR and HR were published by Emergeo WG (2016), and for the Norcia earthquake they are retrieved from Villani et al. (2018). Analyzed data (mean value and 90% confidence interval) are available in Table S1 (Amatrice earthquake) and Table S2 (Norcia earthquake). Horizontal bars indicate areas where the fractures developed: at the contact between the bedrock and the slope deposits, colluvium-eluvium (SDCE; in blue), or within the SDCE (in red). The Pz-points (black points reported in c and f) are at the intersection between the s4- and the ry-profiles (see Figure 4). The modeled gravity-induced displacement (D_{MOD}) were calibrated with the D_{OBS} around the Pz-points (black lines in c and f).

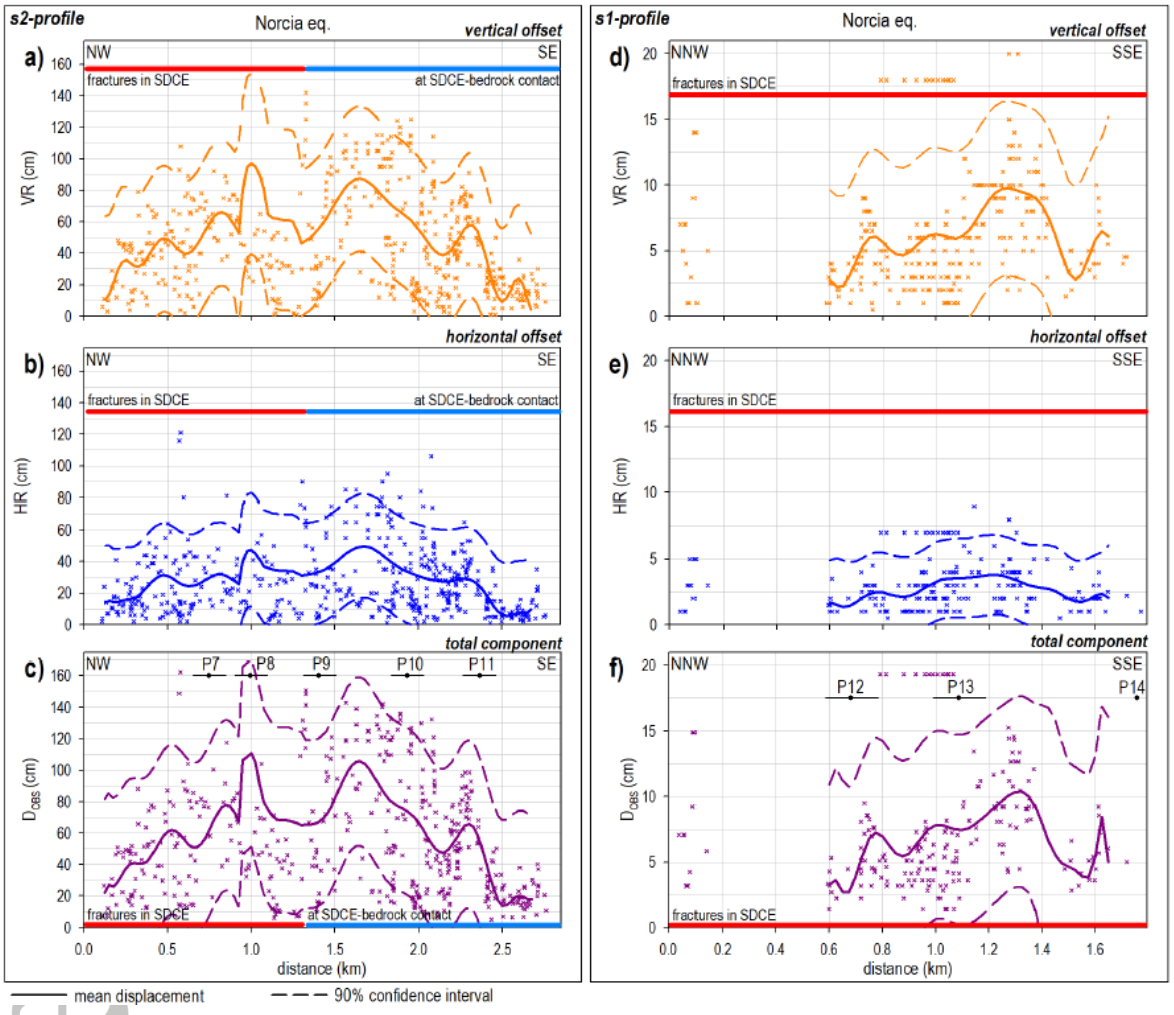

Figure 6. Plot of measured (crosses) and interpolated (lines) vertical (VR; a and d), horizontal (HR; b and e), and total offset (D_{OBS}; c and f) for the coseismic fractures measured after the Norcia earthquake along the s2-profile (a-c) and s1-profiles (d-f) (see Figure 4 and Figure S2). The abscissa reports the distance in km from the northern tip of the sy-profiles and their lengths depict the final deformation zone, resulting from the cumulative effects of the Amatrice and Norcia earthquakes. The measured VR and HR are retrieved from Villani et al. (2018). Analyzed data (mean value and 90% confidence interval) are available in Tables S4 (s2-profile) and Table S6 (s1-profile). The Pz-points (black points in c and f) are at the intersection between the s2- and the ry-profiles (see Figure 4). The reader is referred to Figure 5 for other symbols.

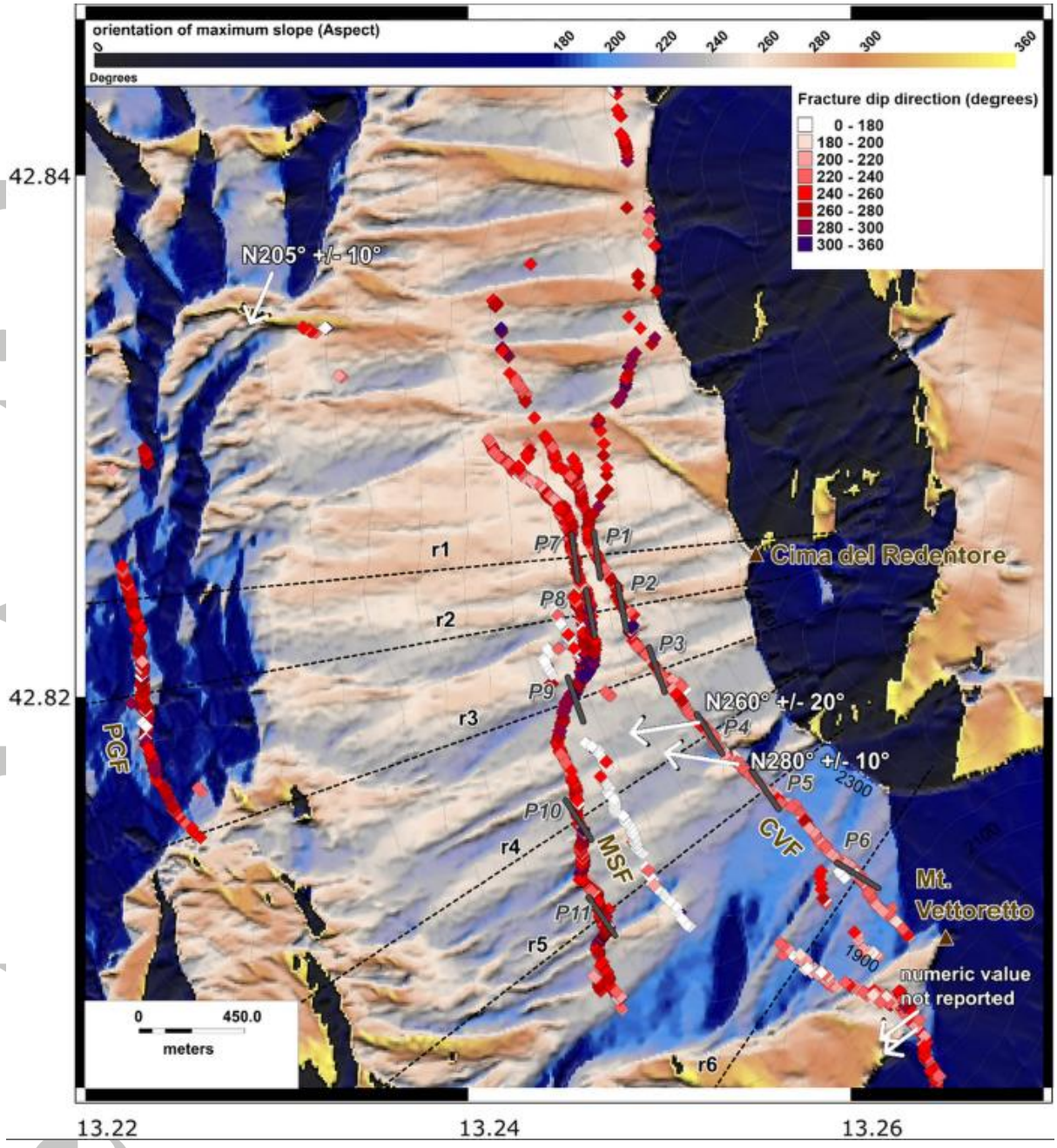

Figure 7: Maximum slope orientation (aspect) analysis for a 10 m resolution digital elevation model (Tarquini et al., 2012) with respect to the fracture dip-direction relative to Norcia earthquake for the western slope of Mt. Vettore. The grey bars represent the 200 m buffer zones across the intersection of sx- and ry-profiles used for statistical analysis of fracture dip-direction (Table 2 and Figure S5; data extracted from Villani et al., 2018). The white arrows with direction values report the measured movement vectors by Perouse et al. (2018) always relative to the Norcia earthquake. Note a good correspondence between the aspect value with respect to the measured slip vector angles (Perouse et al., 2018) and fracture dip-direction. Note that the dip direction of fractures along the upper section of the southern MSF (roughly corresponding to s3-profile in Figure 4 and Figure S2) in the database is reported to be towards NE (see the white colored symbols that depict dip direction in the N0°-N180°range). This data is in contrast with photographic material that shows SW dipping fractures; we refer the reader to Figure 2i (photograph number 58 in Emergeo Working Group, 2017b). The results presented here for the Norcia earthquake are comparable with Amatrice earthquake ones (Fig. S4).

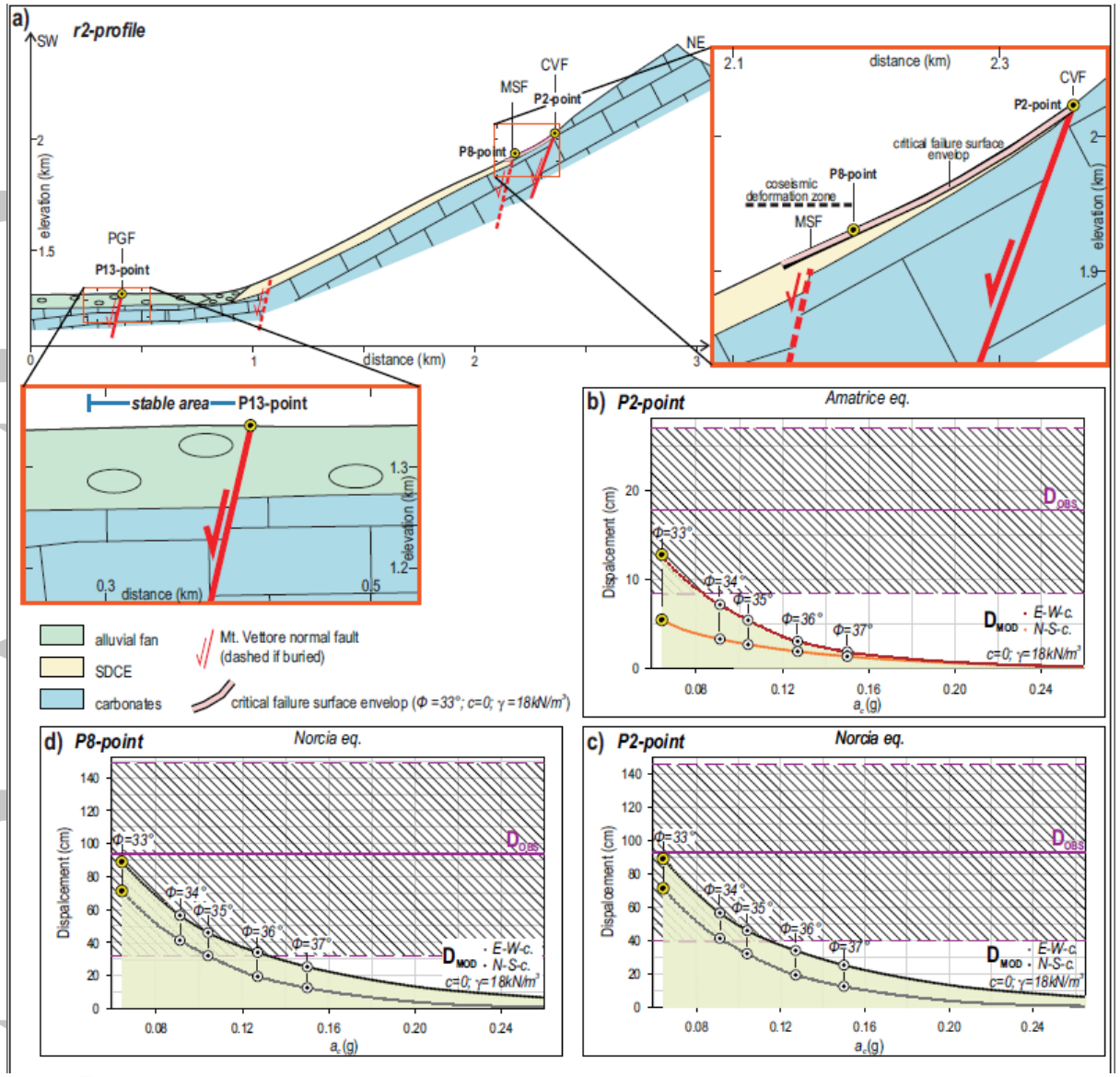

Figure 8. Example of data analysis and modeling along the r2-profile (see Figure 4). (a) Geological cross-section and close-up of the unstable zone along CVF and MSF (right side) and of the stable zone around PGF (lower side). The pink line encloses the critical failure surfaces derived by the LEM analysis for cohesion *c* null and frictional angle ϕ equals to 33° (see this section and Text S1 for more details of slope models and Table S7 for the 2D-geological model). (b-d) modeled gravity-induced displacement (D_{MOD}) obtained using the E-W component (red and grey points) and the N-S component (orange and black points) of strong motion data in the Newark analysis. D_{MOD} is compared with the total component of the observed displacement (D_{OBS}) around the P2-point for the Amatrice (b) and Norcia (c) earthquakes, and around the P8-point for the Norcia earthquake (d). The colored area under the top D_{MOD} curve encloses the D_{MOD} for all tested geological models (Table 1). The white points highlight the D_{MOD} for SDCE at different ϕ and *c* null; the yellow points refer to the geological model in (a). The continuous hatched area encloses the D_{OBS} along with its mean value (the dark pink line) and its 90% confidence interval (dashed lines) (see also P2- and P8-points in Figure 5c, Figure 5f and Figure 6c; data available in Tables S1-S2 and Table S4).

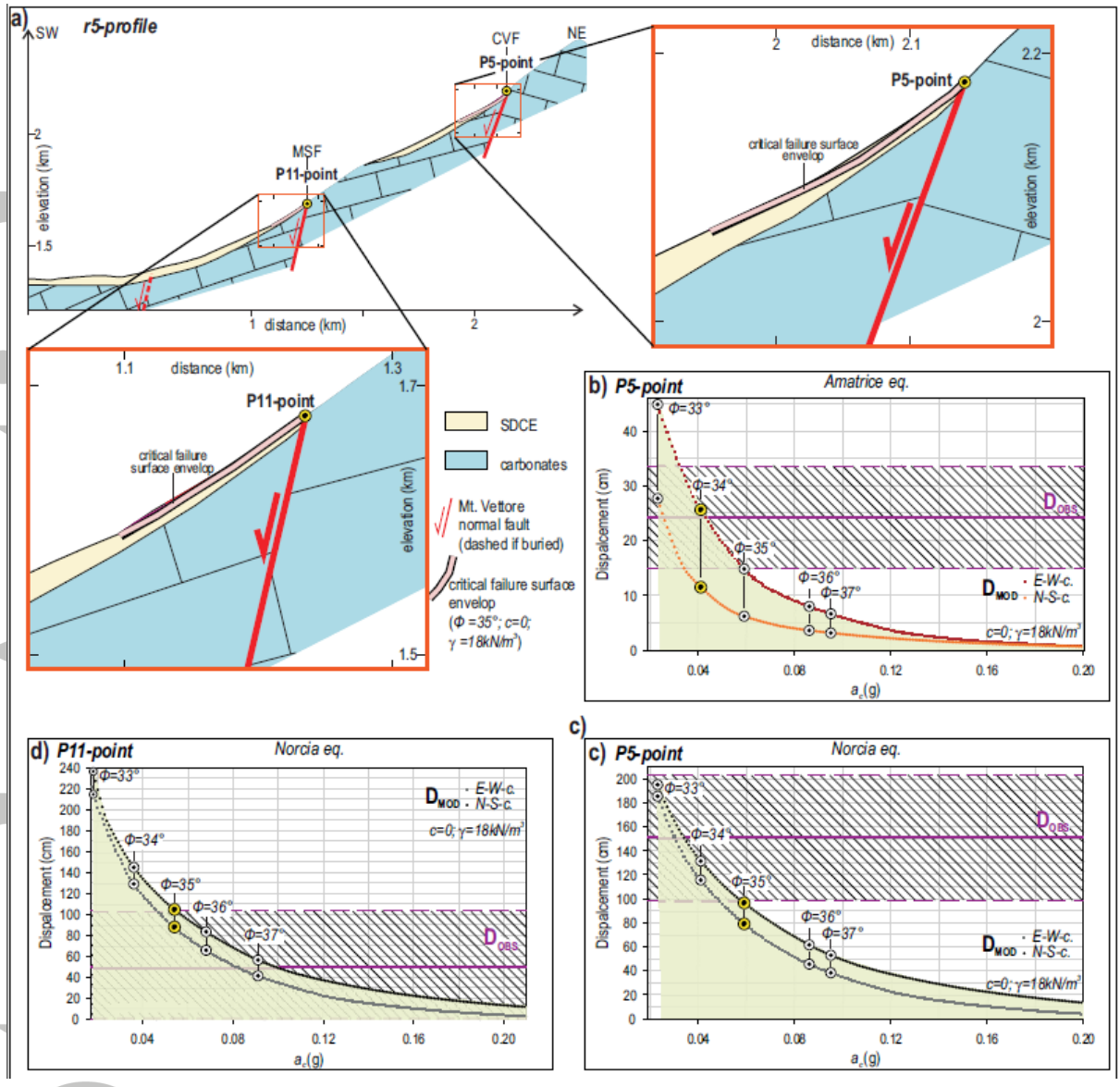

Figure 9. Example of data analysis and modeling along the r5-profile (see Figure 4). (a) Geological cross-section and close-up of the unstable zone along CVF (right side) and MSF (lower side). The pink line encloses the critical failure surfaces derived by the LEM analysis for cohesion (*c*) null and frictional angle (ϕ) equals to 35° (see this section and Text S1 for more details of slope models and Table S7 for the 2D-geological model). (b-d) modeled gravity-induced displacement (D_{MOD}) obtained by Newark analysis compared with the total component of the observed displacement (D_{OBS}) around the P5-point for the Amatrice (b) and Norcia (c) earthquakes, and around the P11-point for the Norcia earthquake (d). The D_{OBS} data are available in Tables S1-S2 and Table S4 (see also P5- and P11-points in Figure 5c, Figure 5f and Figure 6c). The reader is referred to Figure 8 for other symbols.

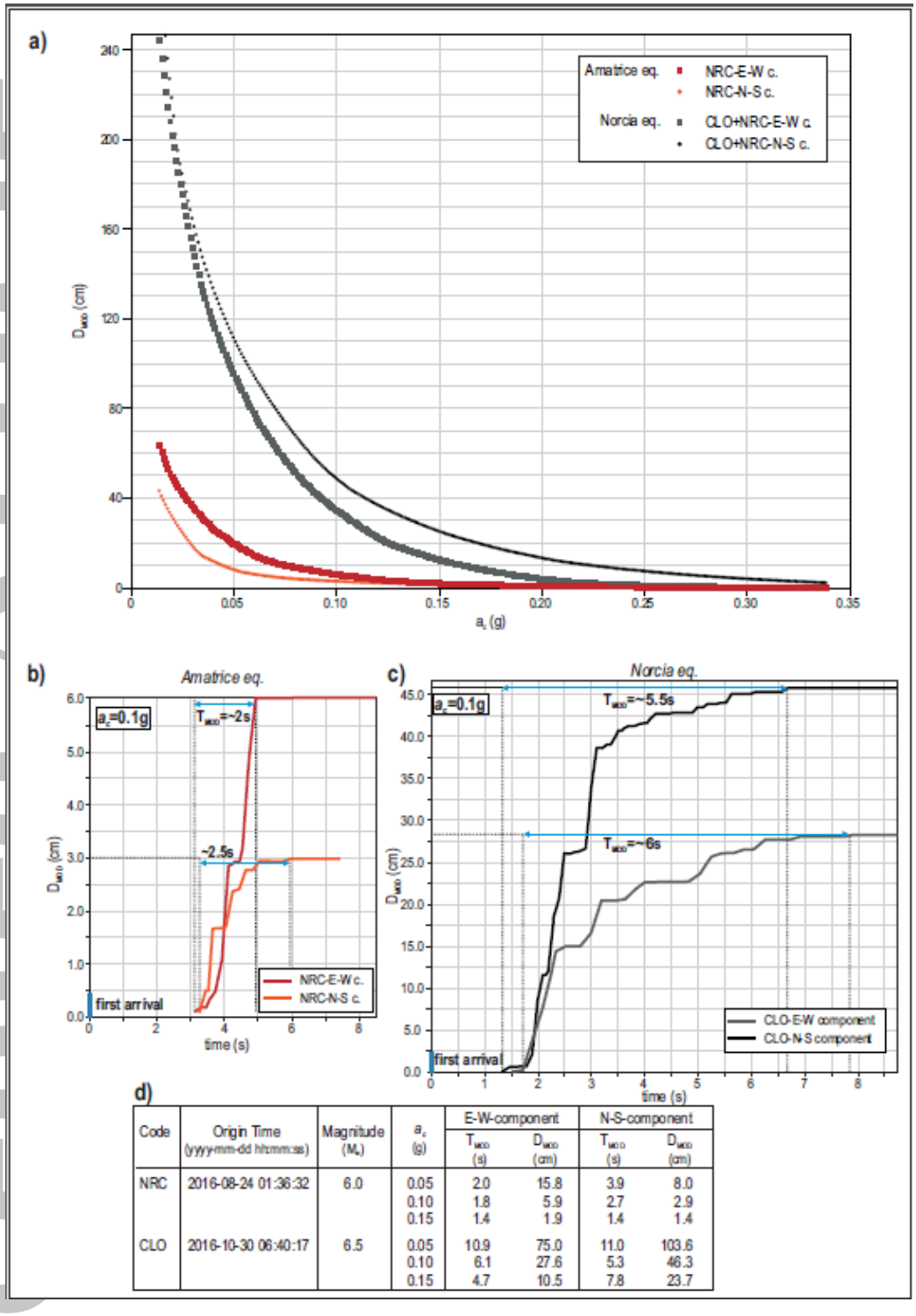

Code	Origin Time (yyyy-mm-dd hh:mm:ss)	Magnitude (M_L)	a_c (g)	E-W-component T_{MOD} (s)	E-W-component D_{MOD} (cm)	N-S-component T_{MOD} (s)	N-S-component D_{MOD} (cm)
NRC	2016-08-24 01:36:32	6.0	0.05	2.0	15.8	3.9	8.0
			0.10	1.8	5.9	2.7	2.9
			0.15	1.4	1.9	1.4	1.4
CLO	2016-10-30 06:40:17	6.5	0.05	10.9	75.0	11.0	103.6
			0.10	6.1	27.6	5.3	46.3
			0.15	4.7	10.5	7.8	23.7

Figure 10. (a) Plot of modeled gravity-induced displacement (D_{MOD}) vs. critical acceleration (a_c) for all modeling (Table 1) along all ry-profiles (Figure 4). The used seismic inputs are the E-W (red and grey points) and the N-S component (orange and black points) of accelerograms recorded at the NRC-station (red and orange points) for the Amatrice earthquake and at the CLO- and NRC-stations (black and grey points) for the Norcia earthquake (see Table 3 for details on the seismic stations and Figure 1a for their locations). (b-c) Plot of time history at 0.1 g (a_c) for the records at the NRC-station (Amatrice earthquake) (b), and at the CLO-station (Norcia earthquake) (c). t=0 s corresponds to the earthquake first arrival and T_{MOD} to the time necessary to produce the complete displacement. (d) Table of maximum D_{MOD} and T_{MOD} obtained at different a_c and for both earthquakes.

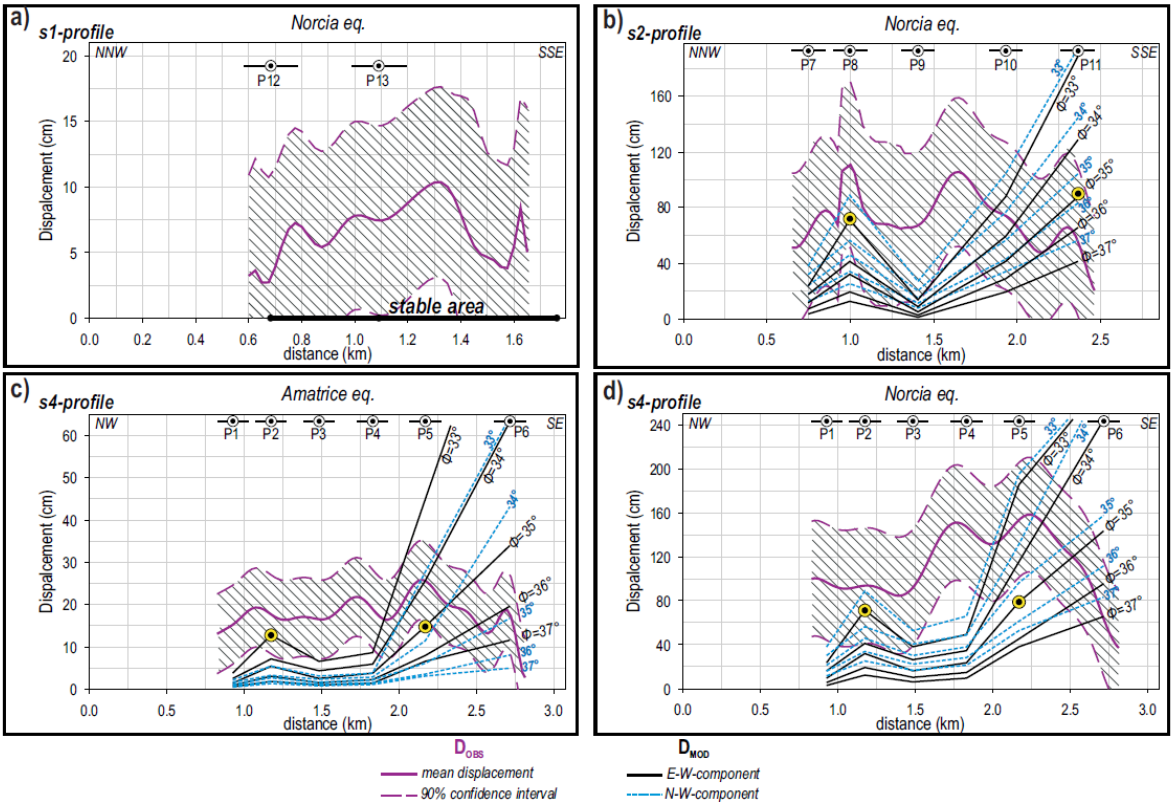

Figure 11. Plot of displacement along the s1- (a) and s2-profiles (b) for the Norcia earthquake, and along the s4-profile for the Amatrice (c) and Norcia (d) earthquakes (see Figure 4 and Figure S2 for location). The abscissa reports the distance in km from the northern tip of the sy-profiles and their lengths depict the final deformation zone, resulting from the cumulative effects of the Amatrice and Norcia earthquakes. The D_{OBS} represents the total component of displacement observed in the field after both earthquakes. The continuous hatched area encloses the mean value of D_{OBS} (dark pink line) and its 90% confidence interval (dashed lines). The analyzed data are available in Table S6, Table S4 and Tables S1-S2, for a, b, c and d plots, respectively. D_{MOD} is the modeled gravity-induced displacement obtained using the E-W component (black lines) and the N-S component (dashed blue lines) of strong motion data at different frictional angles and for null cohesion (the reader is referred to Figures S6-S7 for results at different cohesions). The Pz-points (black points in b-d) are at the intersection between the sx- and ry-profiles. D_{MOD} is compared to D_{OBS} around the Pz-points (black lines in b-d). The yellow points refer to the example points in Figures 8 (P2- and P8-points) and Figure 9 (P5- and P11-points).